Defects in single ice crystals - Influence of surface preparation

von

Markus Batzer

Bachelorarbeit in Physik
vorgelegt dem Fachbereich Physik, Mathematik und Informatik (FB 08)
der Johannes Gutenberg-Universität Mainz
am 26. November 2018

1. Gutachter: Jun.-Prof. Dr. Markus Mezger
2. Gutachter: PD Dr. Martin Jourdan

Ich versichere, dass ich die Arbeit selbstständig verfasst und keine anderen als die angegebenen Quellen und Hilfsmittel benutzt sowie Zitate kenntlich gemacht habe.

Ort, Datum	Markus Batzer

Markus Batzer
AK Butt
Max-Planck Institut für Polymerforschung
Ackermannweg 10
D-55128 Mainz
mbatzer@students.uni-mainz.de
batzer@mpip-mainz.mpg.de

Table of contents

Table of contents

1. Abstract

Ice plays an important role for all organism on earth because the average temperature depends sensitively on the amount of snow and ice due to the equilibrium between received radiation of the sun and re-reflected radiation. One would think that ice is fully understood because H_2O is one of the simplest molecules in chemistry. However, the ice phase Ih is forming an open *Wurzit structure* by hydrogen bounds. In addition, the O atoms are ordered but the hydrogen atoms are disordered on a longrange scale. Depending on the temperature and pressure 18 different ice phases have been observed yet [1].

The aim of this thesis is to investigate the influence of surface preparation on ice single crystal. According to Bilgram from the year 1973 [2], ice single crystals are disturbed up to 1 cm below the surface by mechanical treatment. Based on the doctoral thesis from Schöder [3] an established surface preparation method is to cut the ice by thermal radiation. Therefore, the challenge is to investigate and to compare two preparation methods: The mechanical surface preparation by [4] and the thermal one.

In the framework of this thesis, a wire setup was developed in order to cut ice Ih by a hot wire. The crystal perfection will be investigated by using X-ray Diffraction (XRD). Furthermore, a rocking curve of three mechanical prepared ice samples were recorded with the XRD setup developed by Markus Mezger. In addition, also one thermal treated ice surface was measured. As a reference, the Si (1 1 1) plane was used.

It turned out that the mechanical treated ice single crystals had more defects than the thermal treated one. The so called grain boundaries were clearly visible in the data of the mechanical prepared ice crystals. On the contrary, the ice surface of the thermally treated ice crystal had similar properties as the perfect single Si crystal. Furthermore, the shift of the melting points of the crystallites within the ice crystal based on the Clausius–Clapeyron relation were calculated. It has shown that the crystallites were more compressed for the mechanical treated samples than for the thermally cut ice single crystal.

2. X-Ray Diffraction

Scattering methods are established tools to investigate the structure of condensed matter. In general, *X-ray Absorption* and Scattering are caused by the interaction between X-rays and matter. One speaks of *diffraction* when the observed matter is a crystalline solid. This chapter starts with a introduction of the *kinematic* and *dynamic* scattering theory. Finally, the structure of the ice phase Ih will be introduced.

2.1. Conventions

In the present thesis several conventions will be used for physical quantities or abbreviation. The conventions are listed in Table 2.1. The electrical current is denoted with j to prevent risk of confusions with the beam intensity I. Only very small angular ranges[1] are treated in this thesis. Hence, the more convenient second of arc unit is used.

2.2. Kinematic Diffraction

The kinematic diffraction takes only *single scattering events* into account. This simple assumption is used commonly in X-ray diffraction because the scattering cross-section is rather low and the data analysis is kept quite simple compared to the multiple scattering events in dynamic diffraction. From a quantum mechanical point of view the scattered X-ray beam is only the result of the perturbation of the incident wave since the largest contribution of the intensity is going through the material. This phenomena is known as the *first Born approximation* which assume a weak-scattering between light and material [5].

2.2.1. Scattering amplitude

According to [6, p. 151] one can describe the scattering amplitude from a crystal as following

$$F^{crystal}(\mathbf{q}) = \sum_{l}^{\text{All atoms}} f_l(\mathbf{q}) \mathrm{e}^{i\mathbf{q}\cdot\mathbf{r}_l}. \tag{2.1}$$

The summation is over all atoms within the *unit cell*[2] of the crystal. The vector $\mathbf{q}$ is the momentum transfer between the incident and the scattered wave. $f_l(\mathbf{q})$ represents the *atomic form factor*[3] of an atom located at the position $\mathbf{r}_l$ in the lattice. $\mathbf{r}_l$ can be written as $\mathbf{r}_l = \mathbf{R}_n + \mathbf{r}_j$.

[1] On the order of $\frac{1}{100}^\circ$

[2] Unit cell is spanned by three non-linear vectors $\mathbf{a}_i$ [7, p. 22].

[3] The atomic form factor is a measure of the strength of scattered amplitude off an atom[7, p. 55].

Table 2.1.: Conventions used in this thesis

Variable/ Full form	Unit/ Short form	Description/ Definition
X-**R**ay **D**iffraction	XRD	-
Sum **F**requency **G**eneration	SFG	-
$\lvert\mathbf{k}\rvert = \frac{2\pi}{\lambda}$	m^{-1}	X-ray wave vector
$\lvert\mathbf{x}\rvert$	x	Vector norm of $\mathbf{x}$
$\mathbf{q}$	m^{-1}	Reciprocal lattice vector or momentum transfer
U	V	Electrical voltage
j	A	Electrical current
L_F	$\mathrm{J\,kg}^{-1}$	Heat of fusion
c	$\mathrm{J\,kg}^{-1}\,\mathrm{K}^{-1}$	Specific Heat capacity
I	$arb.unit$	Beam intensity in arbitrary units
Full **W**idth at **H**alf **M**aximum	FWHM ($''$)	Width of a profile at half the maximum
arcsecond	arcsec ($''$)	$1'' \mathrel{\widehat{=}} \frac{1}{60}' \mathrel{\widehat{=}} \frac{1}{3600}^{\circ}$
$(h\,k\,i\,l)$	$(h\,k\,.\,l)$	Short form of the hexagonal miller indices
pixel	px	Pixel of the detector
E	Pa	Young's modulus
$\varnothing$	m	Diameter
Center **o**f **R**otation	CoR	Fixed point during a rotation

The lattice vector $\mathbf{R}_n$ in real space can be expressed as a linear combination of three non-linear vectors $\mathbf{a}_i$ in the form $\mathbf{R}_n = \sum_i n_i \mathbf{a}_i$. The vector $\mathbf{r}_j$ is the position of an atom within the unit cell. Thus, the scattering amplitude (2.1) can be written in the following form

$$F^{crystal}(\mathbf{q}) = \sum_{\mathbf{R}_n+\mathbf{r}_j}^{\text{All atoms}} f_j(\mathbf{q}) \mathrm{e}^{i\mathbf{q}\cdot(\mathbf{R}_n+\mathbf{r}_j)} = \underbrace{\sum_n \mathrm{e}^{i\mathbf{q}\cdot\mathbf{R}_n}}_{(I)} \underbrace{\sum_j f_j(\mathbf{q})\,\mathrm{e}^{i\mathbf{q}\cdot\mathbf{r}_j}}_{(II)} . \tag{2.2}$$

Term (I) describes the summation over the whole lattice. The second term (II) is the so called *unit cell structure factor*. The sum is over one unit cell. Yet, the first term is impractical for further computation because the sum contains roughly 10^{12} terms when assuming an ordinary cubic crystal of the size $1\,\mu m$ on each side [6, p. 153]. This problem will be solved in the next section.

It is worth pointing out that scattering amplitude (2.2) is by definition the Fourier transform of the convolution of a lattice function and a basis function. At first, this may seem to contradict with the derived scattering amplitude since (2.2) is a decomposition of a lattice and a basis

term and not a convolution. The apparent contradiction can be solved by the convolution theorem $\mathcal{F}\{f * g\} = \mathcal{F}\{f\} \cdot \mathcal{F}\{g\}$ [8, p. 52]. This theorem states that the Fourier transform of a convolution is equal to the product of the Fourier transformed functions.

2.2.2. Laue equation

The computation problem in (2.2) can be solved when the phase ϕ of each summand $e^{i\phi}$ is a multiple of 2π. Thus, the sum simplifies to $\sum_{n=1}^{M} e^{i2\pi n} = M$. Therefore, the condition for all phases has to be

$$\mathbf{q} \cdot \mathbf{R}_n = 2\pi n \tag{2.3}$$

where n is an arbitrary integer. Analogously to the real space lattice vector one can define a lattice with basis vectors $\mathbf{b}_i$ in the reciprocal space. The condition (2.3) is fulfilled when all pairs of basis vectors $(\mathbf{a}_i, \mathbf{b}_j)$ satisfy the relation $\mathbf{a}_i \cdot \mathbf{b}_j = 2\pi\delta_{ij}$ where $i, j = 1, 2, 3$ and δ_{ij} is the *Kronecker delta*. Or to put it in other words: the vectors are either parallel or perpendicular to each other. One can solve the computation problem by defining a reciprocal lattice vector

$$\mathbf{G} = h\mathbf{b}_1 + k\mathbf{b}_2 + l\mathbf{b}_3 \tag{2.4}$$

where $(h\ k\ l)$ are the *Miller indices*[4]. Consequently, the scalar product between $\mathbf{G}$ and $\mathbf{R}_n$ in (2.3) leads to

$$\mathbf{G} \cdot \mathbf{R}_n = 2\pi\,(hn_1 + kn_2 + ln_3)\,. \tag{2.5}$$

Obviously, (2.5) and (2.3) are equal since a sum of integers is again an integer. Therefore, the scattered amplitude does not vanish if and only if $\mathbf{q}$ is equal to a reciprocal lattice vector $\mathbf{G}$. Fig. 2.1a shows an illustration of the Laue condition where the initial vector $\mathbf{k}$ hits the atomic plane by an angle θ. The reflected vector $\mathbf{k}'$ with exit angle θ exits only if the so called *Laue condition*

$$\mathbf{q} = \mathbf{G} = \mathbf{k} - \mathbf{k}' \tag{2.6}$$

is fulfilled. It is appropriate to clarify that a reflection can be detected if each component of (2.6) is valid. Therefore, it turns out that a reflection on a crystal can be difficult to find and complicated rotations of the crystal are necessary[10, p. 21].

2.2.3. Bragg's law

Bragg diffraction is the constructive interference of two monochromatic light beams after the reflection at families of planes in a crystal. The requirement for the following process is that the wavelength of the incident rays has to be in the same magnitude as the structure to be investigated. The illustration in Fig. 2.1b shows a lattice structure with a lattice constant d_{hkl}. The $(h\ k\ l)$ plane is penetrated by two coherent parallel X-ray beams (I and II) with wavelength λ at an angle θ. The X-rays are scattered elastically by the atoms at a scattering angle θ. Thus, the two beams have been traveled different distances within the crystal. According to simple trigonometry, it is easy to see that the path difference between beam I and II is twice

[4] The Miller indices indicate the family of lattice planes $(h\ k\ l)$ that are perpendicular to $\mathbf{G}$ [9, p. 863].

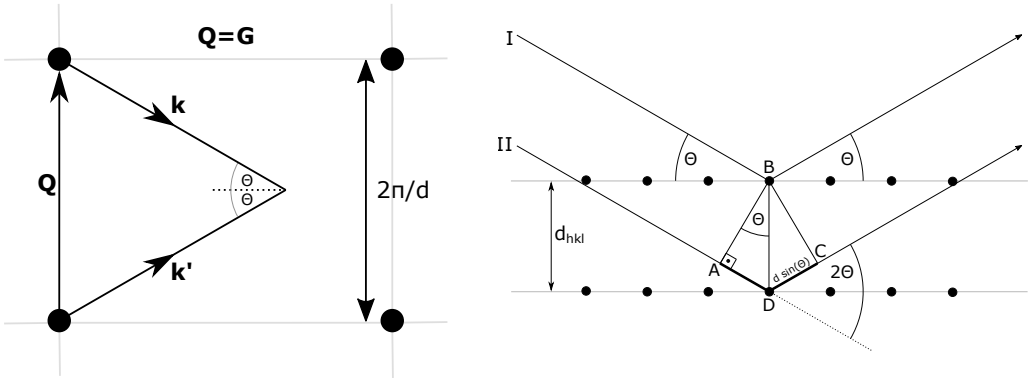

(a) Laue condition in a reciprocal lattice

(b) Bragg diffraction in a lattice structure

Figure 2.1.: Laue and Bragg condition in a 2D crystal structure

$d \sin(\theta)$. Furthermore, the condition for a constructive interference is that the path difference is an integer multiple of λ. Therefore, Bragg's law reads as follows

$$n\lambda = 2d \sin(\theta). \tag{2.7}$$

Bragg's law is the fundamental equation in kinematic diffraction [11, p. 281-282].

For the sake of completeness, it can be shown that the Laue condition and the Bragg reflection are equivalent. The former one is described in reciprocal space whereas the latter one is valid in real space. A proof can be read in [6, p. 155-157].

2.2.4. Ewald sphere

The *Ewald sphere construction* is used for the visualization and geometrical solution of a diffraction problem in the 3D reciprocal crystal. For a better overview, the construction will be explained in two dimensions, i.e. for a so called *Ewald circle*.
Firstly, the monochromatic incident beam $\mathbf{k}$ is drawn from point A to the origin O in the crystal (see Fig. 2.2). Secondly, a circle is constructed by rotating $\mathbf{k}$ around A. Apparently, point B is intersected by the circle which means that the Laue condition (2.6) is valid since the momentum transfer $\mathbf{q}$ is equal to a reciprocal lattice vector $\mathbf{G}$. Hence, a reflected beam can be observed in the direction of $\mathbf{k}'$. By rotating the crystal or, equivalently, by rotating the Ewald circle around O other reciprocal lattice points can lay on the circle. Consequently, other reflections can be observed. It should also be noted that several reflections at the same time can occur since more than one lattice point can be intersected by the circle.

However, in reality, the incident beam is not perfectly monochromatic. Therefore, the circle has a finite thickness $\Delta\mathbf{k}$ (see Fig. 2.2). Thus, the Laue condition is valid for all lattice points within the broadened circle. In an analogous manner the Ewald sphere construction can be applied on a three dimensional crystal [6, p. 161-164].

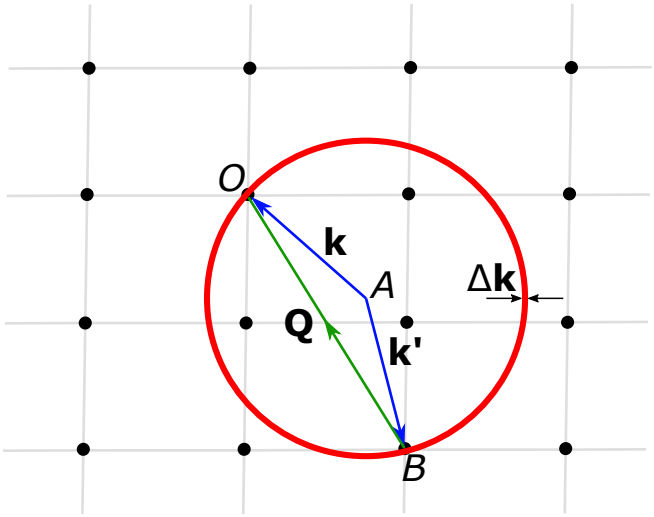

Figure 2.2.: Ewald construction in a reciprocal lattice

2.3. Dynamic Diffraction

The kinematic Diffraction is an established approximation in X-ray diffraction, however, the deficits should also be named. Firstly, the interaction between incident and scattered waves is not treated. Moreover, multiple scattering events are neglected [12]. Secondly, the kinematic theory does not consider all physical allowed reflections in the crystal. The size of the crystal is reciprocally proportional to the size of the reflections spots. Therefore, a perfect periodic crystal would have point size reflection domains in the Fourier space. Consequently, if the circle of the Ewald sphere (see Fig. 2.2) is not overlapping with the infinite small lattice, no peak is observable according to the kinematic Diffraction. But taking into account the *zero point oscillation*[5] the reflection spots would increase and more reflections could be detected [14]. Thirdly, the absorption of the rays inside the crystal. After passing several layers the incident energy has already been attenuated by the layers above [14].

The kinematic Theory is neglecting the interaction of the incident and the scattered waves since the amplitudes of the scattered waves is small compared to the incident ones. However, this statement is not true for a perfect crystal. All scattered waves are in phase due to the coherent lattice. Thus, the interaction of the total scattered wave with the incidental wave cannot be neglected anymore. Such perfect crystals can be obtained for instance from semiconductors such as germanium (Ge) or silicon (Si) [15, p. 111].

Furthermore, the *active scattering volume* of a perfect crystal is much smaller than one would assume when taking into account the photoelectric absorption. If a wave traverse n layers of a crystal its amplitude is attenuated due to reflection with the layers above. The wave can be double reflected in between layer n and $n+1$. Thus, the phase is shifted by π. The superposition between the double reflected wave and an incident wave attenuate the amplitude of the already reduced incident wave. This effect is known as *extinction* and reduces the

[5] Oscillation of the atoms around there center due to uncertainty principle[13, p. 527].

amplitude much faster than absorption wherefore the absorption can be neglected in a first approximation.

According to Darwin, there is total reflection[6] in the immediate region of the Bragg angles θ, everywhere else the reflected intensity is zero [15, p. 112]. This can be seen in the red curve of the Darwin curve of Si(2 2 0) in Fig. 2.3. For the red curve it was assumed that the intensity runners decrease rapidly against zero. Hence, they can be set to zero. On the contrary, the asymmetric shape of the black curve in the total reflection regime in Fig. 2.3 can be explained by the so called *Anomalous Absorption* or the *Borrmann effect*. According to [14, p. 17-19] the incident wave and the reflected wave in a crystal interfere in such a way that a set of standing waves is produced. Its nodes lie on a plane parallel to the lattice plane. In addition, the periodicity d_{hkl} of the lattice plane is equal to the periodicity of the nodes. The absorption strength depends on the phase ϕ between incident wave and scattered one. For the case $\phi = \pi$ the nodes lie on the atoms which leads to a small absorption. However, for $\phi = 0$ the maximum of the standing waves lie on the atoms and the absorption is high. Obviously, for phases $0 < \phi < \pi$ the absorption decreases continuously from π to 0. The explicit formula for the integrated intensity can be found in [16].

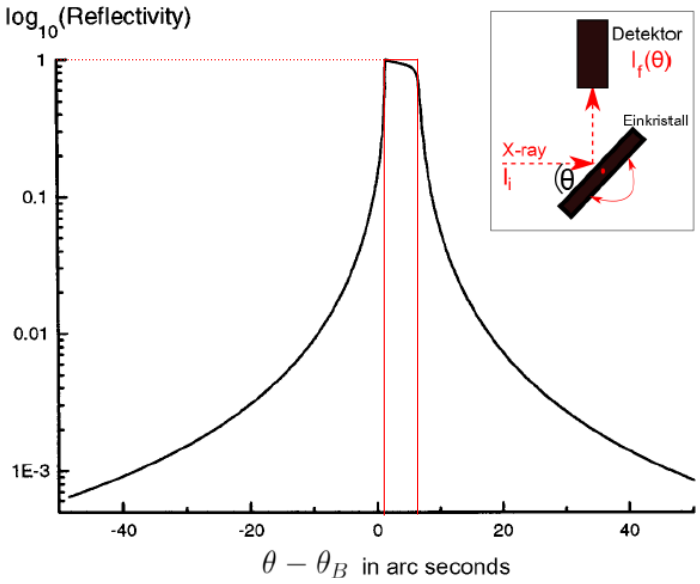

Figure 2.3.: Darwin curve of a Si (2 2 0) single crystal for $CuK_{\alpha 1}$ radiation. Figure from [17].

2.4. Ice Ih

Ice Ih forms a complex hexagonal lattice with water molecules. It is known from X-ray diffraction and band spectra that each water molecule is surrounded by four other molecules in a tetrahedron [18]. The oxygen atoms are arranged in a so called *hexagonal Wurzit structure*

[6] Neglecting absorption effects[14, p. 101]

(see. Fig. 2.4). First established from J. D. Bernal, and R. H. Fowler in 1933, the *ice rules* or *Bernal-Flower rules* say that each oxygen atom is covalently bounded to two hydrogen atoms to form H_2O. Moreover, each H atom of a water molecule is bonded via hydrogen bound to a further O atom in such a way that on each straight line between two nearest oxygen atoms lays a hydrogen atom in between [19, p. 15-16]. The distance O–O is roughly 2.75 Å and the angle O–O–O is approximately 109° [20]. The unit cell (see blue cell in Fig. 2.4) contains four oxygen atoms. The lengths of the edges are $a = 4.4975$ Å and $c = 7.3224$ Å [21] where the c-axis is perpendicular to the hexagonal face. In the hexagonal lattice one uses three axes in the hexagonal face to ensure the uniqueness of the direction.[7] All three a-axes are orientated along one corner of the hexagonal face, respectively. Furthermore, each pair of axes are separated by an angular distance of 120°.

Further description of the structure of ice Ih will be explained through Fig. 2.5 due to

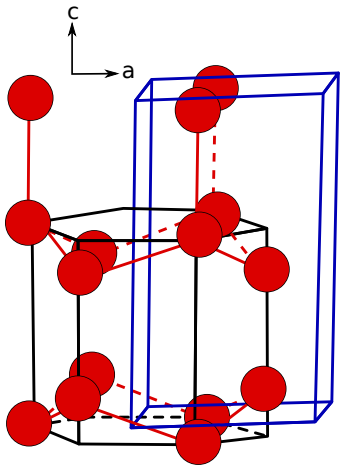

Figure 2.4.: Hexagonal crystal structure (black) of oxygen atoms (red) plus the unit cell (blue) of ice Ih [23, p. 7].

an easier approach in the 2D planes compared with the complex 3D structure in Fig. 2.4. For describing a hexagonal lattices one uses four miller indices $(h\,k\,l\,i)$ with the condition $i = -(h + k)$. The basal plane $(0\,0\,0\,1)$ shows that six oxygen atoms forming a hexagonal ring where one half of each O atom belongs to two adjacent hexagons, respectively. Along the c-axis ice Ih is stacked in a ABABAB order.Additionally, the basal plane is constructed by a bilayer which can be seen in the 1st prism plane which is a side face of the hexagon. The 2nd prism plane lays within the hexagon connecting two second nearest corners.

This thesis deals about measuring Bragg reflections of ice Ih. Hence, it is necessary to predict the orientation of the sample. Therefore, rotation angles and the $\mathbf{q}$ vector of some selected lattice planes will be calculated in the following.

Firstly, the angles have to be defined. The corresponding angles can be seen in Fig. 3.1. It should be denoted that the angles given in Fig. 3.1 are named differently than the angles

[7] For further reading see [22, p. 11-12].

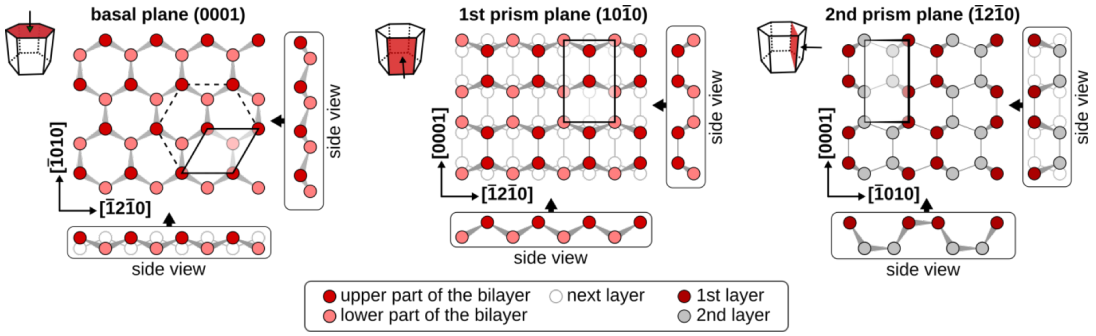

Figure 2.5.: Illustration of hexagonal ice Ih crystal for basal plane (left), 1st prism plane (middle) and 2nd prism plane (right). Figure taken from [4].

in the XRD setup in section 3. For the following calculation the angles in Fig. 3.1 are used. Furthermore, a right-handed Cartesian coordinate system has to be defined in order to calculate the $\mathbf{q}$ vector in the reciprocal space. The z-axis is defined along the c-axis of the hexagonal crystal. Without any loss of generality the x-axis shows along one a-axis. Consequently, the y-axis is set. Thus, the real space basis vectors $\mathbf{a}_1$, $\mathbf{a}_2$ and $\mathbf{c}$ can be expressed by the dimensionless Cartesian unit vectors $\mathbf{e}_x$, $\mathbf{e}_y$ and $\mathbf{e}_z$. Then the transformation in reciprocal space leads to the basis vectors $\mathbf{b}_1$, $\mathbf{b}_2$ and $\mathbf{c}^*$. The complete calculation of the lattice vectors has been left out but can be read in [24, p. 224-225]. However, the lattice vectors in real and reciprocal space are given in Tab. 2.2.

Secondly, the reciprocal basis vectors can be used to generate the reciprocal lattice vector

Table 2.2.: Real and reciprocal lattice vectors of the hexagonal crystal where $\mathbf{e}_x$, $\mathbf{e}_y$ and $\mathbf{e}_z$ are dimensionless Cartesian unit vectors.

Vectors in real space	Vectors in reciprocal space
$\mathbf{a}_1 = a \cdot \mathbf{e}_x$	$\mathbf{b}_1 = \frac{2\pi}{a} \cdot \mathbf{e}_x + \frac{2\pi}{\sqrt{3}a} \cdot \mathbf{e}_y$
$\mathbf{a}_2 = a \cdot \left(\frac{\sqrt{3}}{2} \cdot \mathbf{e}_y - \frac{1}{2} \cdot \mathbf{e}_x\right)$	$\mathbf{b}_2 = \frac{4\pi}{\sqrt{3}a} \cdot \mathbf{e}_y$
$\mathbf{c} = c \cdot \mathbf{e}_z$	$\mathbf{c}^* = \frac{2\pi}{c} \cdot \mathbf{e}_z$

$\mathbf{G}$ as in (2.4). Due to the Laue condition (2.6) is a Bragg reflection occurring if and only if $\mathbf{q} = \mathbf{G}$ holds. The $\mathbf{q}$ vector can be split in a component perpendicular to the basal plane $\mathbf{q}_\perp$ and a parallel component $\mathbf{q}_\parallel$[8]. These components can be calculated by projecting $\mathbf{q}$ on each Cartesian axes. Moreover, also the angles δ, ω, χ and ϕ can be obtained by the projections.

Thirdly, the d-spacing d_{hkl} for a given $(h\,k\,.\,l)$ can be calculated with the *quadratic Bragg equation* (2.8) from [10, p. 28]. Apart from this, one can obtain the expression (2.9) by

[8] $\mathbf{q}_\parallel$ is defined as $\mathbf{q}_\parallel := \mathbf{q}_x + \mathbf{q}_y$.

inserting Bragg's law (2.7) into (2.8). Thus, one receives (2.9) for calculating the 2θ value.

$$\frac{1}{d^2} = \frac{4}{3}\left(\frac{h^2 + hk + k^2}{a^2}\right) + \frac{l^2}{c^2} \tag{2.8}$$

$$\overset{(2.7)}{\Longleftrightarrow} \sin^2(\theta) = \frac{\lambda^2}{4}\left(\frac{4}{3}\left(\frac{h^2 + hk + k^2}{a^2}\right) + \frac{l^2}{c^2}\right) \tag{2.9}$$

The estimated values can be found in Table 2.3. Table A.4 shows the same values but for the angles declaration used in the XRD setup from section 3 on.

Table 2.3.: Calculated angles and **q** components for selected (hk.l) planes from [4]. The d-spacing values are taken from [21].

Reflection plane	$2\theta(^\circ)$	d_{hkl}(Å)	q(Å^{-1})	$q_\parallel$(Å^{-1})	$q_\perp$(Å^{-1})	$\delta(^\circ)$	$\omega(^\circ)$	$\chi(^\circ)$	$\phi(^\circ)$
(0 0 . 2)	24.29	3.66	1.716	0	1.716	12.15	12.15	0	–
(1 0 . 5)	68.38	1.37	4.584	1.613	4.290	54.80	0	0	0
(1 0 . 5)	68.38	1.37	4.584	1.613	4.290	54.80	0	0	60
(1 0 . 0)	22.81	3.89	1.613	0	1.613	11.41	11.41	0	–
(2 0 . 0)	46.60	1.95	3.226	0	3.226	23.30	23.30	0	–
(2 0 . 1)	48.32	1.88	3.338	0.858	3.226	39.05	9.27	0	180
(1 1 . 0)	40.06	2.25	3.338	0.858	3.226	39.05	9.27	0	180

3. Experimental Setup

The content of this chapter is the description of the experimental setup, including the Bartels monochromator. In addition, the in-house developed wire setup for preparing the ice surface is explained.

3.1. Diffractometer Geometry

As previously stated in section 2.2.2 the crystal has to be rotated complexly with respect to the incident beam. The rotations can be accomplished by a so called *six-circle diffractometer*. One example of such a diffractometer can be seen in Fig. 3.1. In this connection, it should be mentioned that the sample surface is prepared in such a way that a certain ($h\ k\ l$) plane is parallel to the sample surface. This approach is useful since this plane is already measurable when sample surface is aligned parallel to the beam. This ($h\ k\ l$) plane is used as a reference plane since the tilting angles between two lattice planes can be calculated. The initial state (see Fig. 3.1a) is distinguished by the fact that the sample surface is parallel to the incident beam and in the center of rotation. On the contrary, Fig. 3.1b shows a reflection state where all circles are orientated to observe the reflection from a desired lattice plane.

3.2. XRD Setup

The Bragg peaks of ice Ih were measured with the six-circle diffractometer setup which can be seen Fig. 3.2. It should be stated that the X-ray source, two slits, the filter and the tube are located in vacuum due to decrease undesirable air scattering. The vacuum pressure is below 20 mbar. The reflections of Si (1 1 1) were acquired without the sample holder (light blue box) on top of the sample tower. However, the remaining setup is the same for Si and ice Ih.

The X-rays are produced by a rotating anode X-ray generator (*Rigaku*). The rotating anode is operated with 40 kV and 20 mA. The energy of the out coming X-ray is 8.04 eV. The corresponding wavelength is 1.54 Å. The beam is propagating along the x-axis and has roughly a width of $500 \times 800 \mu m^2$. Afterward, the beam is entering the 4-jaw monochromator slit (ms) system . The slit system consists of two vertical and two horizontal jaws, respectively. Two parameters can be set for the jaws. Firstly, the gap distance between two jaws located opposite each other. Secondly, one can move the gaps along the vertical or horizontal direction. The next component of the beam path is a filter system. Its function is the attenuation of the incident beam. After the filter the beam is leaving the vacuumed sealed section and is propagating to the next component. Within the next component, the X-rays are reduced in energy width and angular divergence by the so called *Bartels monochromator*. This monochromator will

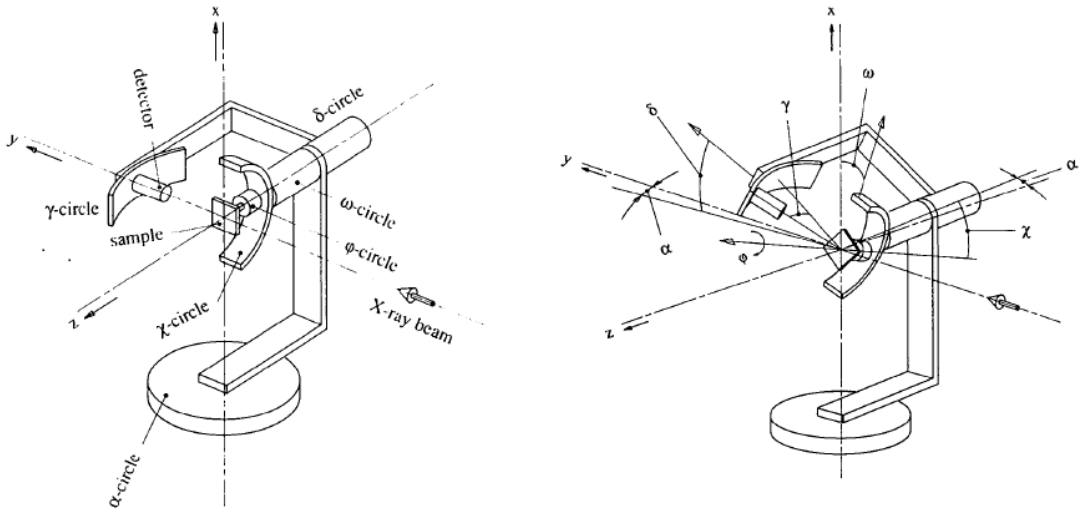

(a) All circles are set to zero position and the beam is parallel to the sample surface.

(b) All circles are shifted from zero position in order to detect a reflection.

Figure 3.1.: Illustrations of a six-circle diffractometer at (a) zero position of all circles and at (b) a reflection position. Figures from [25]

be explained in greater detail in section 3.3. However, the monochromator is only sensitive for horizontal divergences due to the upright alignment of the mirrors. Thereafter, the beam is passing another vacuum sealed entrance slit (es) system. Afterward, the beam is reflected by the sample and is scattered by the angle 2θ with respect to the incident beam. Thus, the beam is traversing the tube and is detected by the linear detector (*Mythen*). The detector area is aligned horizontal. There is an option to install horizontal aligned slits at the entrance and the exit of the tube. These slits have a vertical gap distance in the magnitude of mm. The slits are used for shielding divergent beams along the vertical direction. It should be noted that the two slit systems (ms and es) and the slits at the tube will be discussed more precisely if the alignment of the sample is explained in section 3.4. Furthermore, the linear detector consists out of 1280 px whereas each pixel has a width of 55 µm. Consequently, the total detected width is 70.4 mm. The resolution of the detector is limited by the size of one pixel and the distance between the detector and the sample. All ice samples were measured at a distance of roughly 593 mm. Hence, according to simple trigonometry, one pixel corresponds to an angular resolution of $0.33''$. On the contrary, Si was measured at a distance of approximately 639.5 mm. Thus, the angular resolution of one pixel is $0.31''$.

The top view of the setup can be seen in Fig. 3.2a. The sketch shows a scattering event where the sample tower is rotated by ω with respect to the incident beam. This rotation is performed by the omega (om) stage. Independently from the rotation of the sample tower, the detector is turned by the horizontal two theta (htth) stage by the angle 2θ. The htth stage is responsible for moving the detector on a circle around the sample in the equatorial plane. Consequently, the detector points always to the center of the circle. Moreover, the ice crystal

(drawn in light blue) is located under the orange kapton dome. After the surface preparation the crystal is frozen on a copper disk. This disk is screwed on a thread and then in contact with a second copper disk. The second one in turn is situated in the circuit of a so called refrigerated circulators (*Julabo*). This cooling circuit operates with the cooling liquid isopropyl alcohol C_3H_8O. Hence, the ice is cooled through the interface copper–copper. In addition, the ice crystal is surrounded by dry nitrogen gas N_2 in order to increase the pressure inside the dome. Thus, the kapton foil is streched due to the overpressure inside of the sample holder. However, increasing the background noise with a more suitable but more expensive gas like Helium is not necessary. As it can be seen later, the peak intensities distinguish themselves clearly from the background. For the sake of clarity only the feed of the cooling liquid (in blue) and the nitrogen gas (in green) are drawn in Fig. 3.2a.

However, a side view of the sample tower can be seen in Fig. 3.2b where all angles are set to zero. The functions of the relevant stages are explained in the following whereas the other stages are given for the sake of completeness. The vertical two theta (vtth) stages is a virtual one. The motion of the stage is a combined movement of the detector linear (dlin) stage and the detector rotation (drot) stage. Firstly, dlin drives the detector along the z-axis on a straight line. Thus, the detector is displaced and not pointing in the center anymore. Secondly, the displacement is compensated by a rotation of the drot stage. The result is that the detector is pointing again to the center. Moreover, the omega (om) stage is responsible for the rotation along the z-axis. Above the om stage is the sample z (saz) stage. Its function is to move the sample along the z direction. Directly over it, the chi/phi stage is located. This stage is tilting the sample along a circle within the image plane or perpendicular to the image plane. The center of these circles are situated on the sample surface. The reason why the saz stage is below the chi/phi stage is in order to move the center of each circle on the same height as the sample surface. Finally, the translation movement of the sample along the x and y direction is achieved with the sample x (sax) and sample y s(say) stage. Therefore, it is possible to move the sample surface on the axis of rotation of the om stage. Simultaneously, the center of rotation of the chi and phi stage are also placed on the sample surface. For the measurement of ice there are two additional stages available. The gchi stage rotates the sample along the y-axis whereas the sample is rotated along the x-axis by the gphi stage. Their functions are equivalent to the chi and phi stage when

All stages are controlled by the XRD software *spec*. One can scan each stage within a certain interval, step width and counting time per step, while the detector is counting the intensity at each step. Moreover, one can set different pixel intervals while a scan takes place. These pixel intervals are given in table 3.1 and did not change in this work. The so called *relative scan* makes it possible to scan around the current position of a stage. During this scan several values are registered, in particular the temperature in order to know the temperature of the ice. The sensor is placed inside the sample holder of ice. Each stage in Fig. 3.2 corresponds to a certain angle. In this work the so called *Rocking Scan* is used in order to obtain the rocking curve. It is done by fixing the MY_{R1} pixel of the detector at the center of the Bragg reflection while the om stage is tilting the sample. While only the basal face and the (1 1 1) plane of Si are investigated the usage of the vtth and gphi stage is omitted. Hence, the rotation stages to be used are reduced to the om, htth and gpchi stage since the scattering processes takes place in the equatorial plane. In the follwing, the position of the om stage is characterized by the

angle ω. In addition, the rotation of the htth stage is described by the angle 2θ and the position of the gphi stage is given by the angle ϕ.

Table 3.1.: The defined pixel intervals for the linear detector. The MY_{PB} pixel interval covers roughly the intensity of the primary beam.

Name of the interval	Pixel interval	Function
MY_T	0 – 1279	Counting all 1280 pixels
MY_{PB}	685 – 715	Counting pixels within the primary beam
MY_{R1}	700 – 700	Counting one pixel at the center of the primary beam

3.3. Bartels monochromator

3.3.1. Working Principle

Bartels monochromators, also known as *DuMond-Bartels monochromators*, are used to decrease the energy width and divergence of X-rays based on multiple Bragg reflection. Fig. 3.3 shows the dispersive arrangement of a fourfold Bartels monochromator. This monochromator has two channel-cut crystal[1] pairs (I and II). The crystals in each pair are aligned parallel to each other. The pair II is rotated by the Bragg angle β with respect to the incident beam whereas the other pair is rotated by $-\beta$.

The dispersive arrangement, known as $(+--+)$ arrangement according to [26, p. 113], is required in order that the energy width and the angular divergence of the incident beam decreases. These effects can be explained by Fig. 3.3. The beam path (black line) corresponds to an X-ray with wavelength λ and incident angle β which fulfill the Bragg condition (2.7) at II. Consequently, the X-ray is reflected by II and by I due to the symmetry of the arrangement. But the incident beam is not monochromatic and has an angular divergence. Hence, an X-ray can be reflected by II at an incident angle $\beta' < \beta$ with a wavelength $\lambda' < \lambda$. Thus, this X-ray is not reflected by I because the incident angle is higher than β'. Analogously, this applies also for an X-ray with wavelength $\lambda'' > \lambda$ and an incident angle $\beta'' > \beta$ at pair II. It should be noted that not only the X-rays with λ and reflecting angle β are selected by the monochromator. According to section 2.3, there is a plateau in the magnitude of $10''$ around the Bragg angle. Therefore, the Bartels monochromator selects all rays which fulfill Bragg's law within this plateau. In other words, the wider the plateau the higher the intensity of the out coming beam.

The advantage of a dispersive arrangement in Fig. 3.3 is that the beam is not shifted sideways with respect to the incident beam. Thus, the same alignment of the setup in Fig. 3.2 can be used with or without Bartels monochromator in the beam bath.

The question now is which crystal is suitable for the Bartels monochromator. A comparison of the Si(1 1 1) and the Ge(2 2 0) plane can be seen in Fig. A.1. While Si has a narrower peak (FWHM=$7.36''$) than the (2 2 0) plane of Ge (FWHM=$12.57''$), it is obvious that germanium

[1] The surface a of channel-cut crystal is parallel to a certain lattice plane.

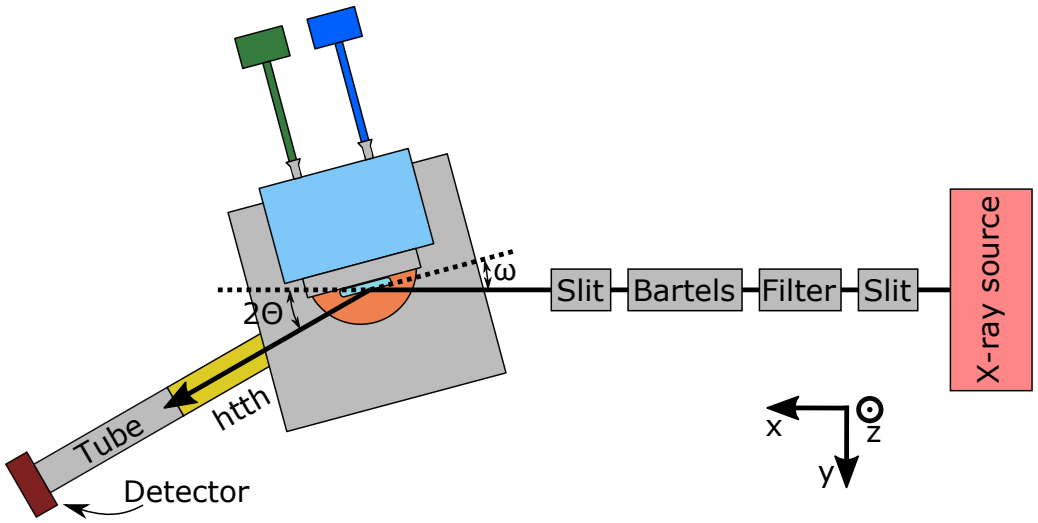

(a) Top view of the experimental setup where sample tower is shifted by ω and the detector tower is rotated by 2θ with respect to the incident beam. The cooling system (drawn in blue) with isopropyl as a cooling fluid and the nitrogen N_2 supply (drawn in green).

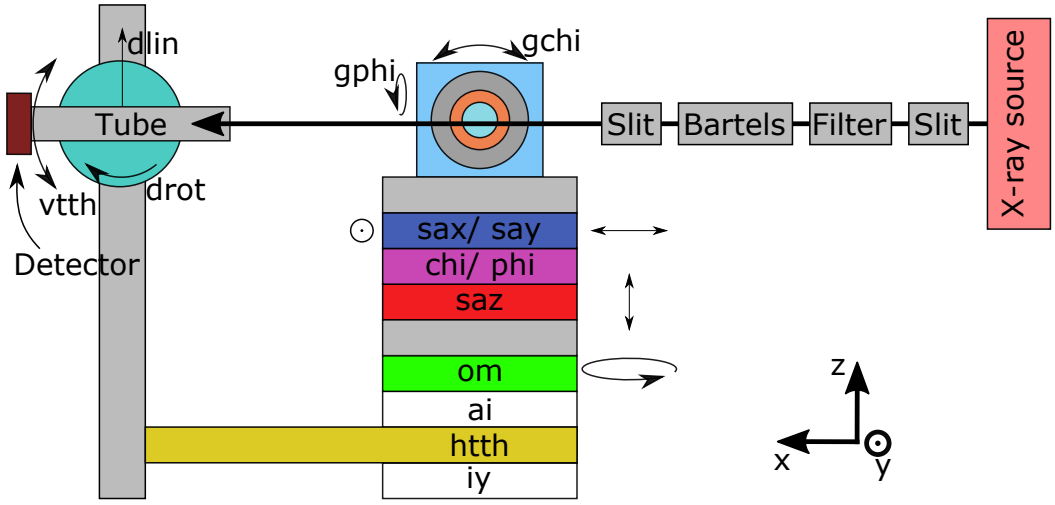

(b) Side view of the experimental setup where $\omega = 2\theta = 0°$.

Figure 3.2.: Experimental setup for XRD of ice Ih from (a) top view and (b) side view. The beam is produced by the X-ray source. Before the beam is scattered by the sample passes through a slit system, filter system, Bartels monochromator and another slit system. The sample (drawn in light blue) is located on top of the sample tower. Afterward, the sample is detected by the linear detector.

is reflecting more beam at its respective Bragg angle. Consequently, less intensity loss is gained when the Bartels monochromator is performed with Ge(2 2 0) planes. Therefore, two pairs of channel-cut Ge(2 2 0) crystals were chosen.

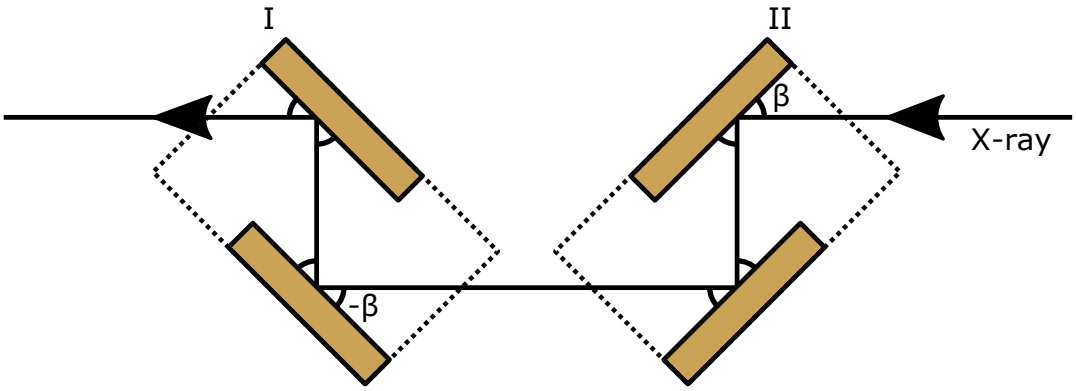

Figure 3.3.: Two crystal pairs (I and II) in a dispersive arrangement represent the Bartels monochromator. Each crystal pair is channel-cut along the same $(h\,k\,l)$ plane. The pair I and II are rotated by the Bragg angle $-\beta$ and β with respect to the incident beam, respectively.

3.3.2. Alignment

Firstly, all angles in Fig. 3.2 are set to zero, in particular the angles of the Bartels monochromator in Fig. 3.3. The two pairs I and II are each located on a slide. Each slide can be moved along the y-direction by the stage cm1y and cm2y, respectively. Furthermore, I and II can be rotated along the z-direction by the stage cm1th and cm2th, respectively. The cm1th and cm2th stages are aligned almost parallel to the beam at their zero position. Moreover, the Bartels monochromator is moved along the y-axis out of the beam path by a the stages cm1y and cm2y. The vertical and horizontal gaps of es and ms are opened to 10 mm. The filter is inside the beam path in order not preserve the detector with too high intensities. Hence, the beam is propagating straight to the detector without a sample in between. In the following the alignment strategy will be explained in order to align II and I parallel to the incident beam. The upper surface of II is shifted to the beam and a relative scan of cm2y is executed. One observes an intensity plateau when the crystal is not in the beam. Then a steady decrease of the intensity is observable when the upper surface is moved gradually inside the beam. Zero intensity is measured if the crystal has reached the position where the beam is completely blocked. The cm2y stage is moved to the edge of this intensity profile. The current position is set to zero. Afterward, a relative scan is performed by the cm2th stage. Hence, most of the beam is blocked when the crystal is tilted. After that the intensity increases linear when the stage is moving to the nominal zero position. At the zero position the intensity has reached its maximum because the crystal is parallel to the beam. While the crystal has passed the zero position the intensity decreases linear. Consequently, the intensity profile has the form of a triangle. Then the cm2th stage is moved to the angle where the maximal intensity was counted. Also this position is set to zero. The relative scans of cm2y and cm2th are repeated as long as the triangle is symmetric. Then the pair is moved out of the beam and pair I is placed in the beam. Analogously to pair II, the upper surface of I is aligned parallel to the beam.

Secondly, the next step is done by shifting II into the beam path and I out of the beam path. As shown in Fig. 3.3, the Ge pair is rotated by its Bragg angle 22.65°[2]. The Bragg condition is fulfilled due to the fact that (2 2 0) plane is parallel to the surface and intensity is measured by the detector. Furthermore the filter has to removed out of the beam in order to increase the intensity. The other pair is placed also in the beam path and is rotated by the Bragg angle −22.65°. Thus, also I fulfill Bragg's law.

Finally, the two pairs have to be aligned to each other due to possible defects or miscuts in the crystals. At first, a relative scan of cm2th is executed and the angle is set where the highest intensity was observed. The same scan is done by the cm1th stage. Afterward, both stages are scanned in the same rotation direction. The final step is a asymmetric rotation scan of the stages. Hence, the cm1th stage is rotated along the positive rotation direction while cm2th is rotated in opposite direction and vice versa. An iteration over the symmetric and antisymmetric rotation is done.

3.3.3. Si(111) Reference Measurement

According to section 2.3, silicon can be grown as an almost perfect single crystal. Therefore, a channel-cut Si(1 1 1) crystal is used as reference measurement. The result will be compared with the measurements of the basal face of ice Ih. The expectation of the rocking curve of Si(1 1 1) can be seen in Fig. A.1b. The curve shows the typical asymmetric shape as describe in section 2.3 due to dynamic effects.

The first step for measuring the rocking curve of Si(1 1 1) is to align the surface parallel to the incident beam. The alignment procedure will be explained in more detail in section 3.4. Secondly, ω is moved to the calculated Bragg angle of 14.22° according to [27]. The detector is moved twice the ω angle to the value $2\theta = 28.44°$. A relative scan of *om* is performed and ω is set to the position at the maximum of the scan. The same is done with 2θ while only the MY_{R1} pixel is used to find the maximum of the intensity. When the peak is found, a rocking curve is taken around the peak. The measured curve can be seen in Fig. 4.1.

3.4. Sample Alignment Procedure

This section contains the general sample alignment procedure. In the following the rotation stages cm1th and cm2th of the Bartels monochromator remain unaffected. If not explicitly mentioned in one of the alignment steps, the adjustment is done by the complete pixel interval MY_T.

Firstly, all angles are set to zero. The sample is moved out of the beam path in order to align the dlin and the drot stage. It is a two dimensional problem when aligning dlin and drot. If neither dlin nor drot is at the correct position no intensity is measured. For that tiny shifts of dlin and drot are necessary in order to orientate the detector almost parallel and to find roughly the correct height. If one finds part of the intensity, relative scans of dlin and drot are measured. After a few iterations of both scans the stages are aligned.

Secondly, the slit system ms will be aligned whereby the gaps of es are opened to 10 mm.

[2] According to [27]

Before the alignment of the slits are explained in the following, the expressions vertical and horizontal gap and the horizontal and vertical offset have to be clarified. The vertical offset is the motion of the vertical aligned jaws along the horizontal direction. Hence, also the vertical gap is moved along the horizontal direction. The horizontal offset and the horizontal gap are doing the opposite. The vertical gap of ms is moved to a small value, e.g. 1 mm and the horizontal one to a large value, e.g. 10 mm. Afterward the offset of the vertical gap is relatively scanned in order to find the position where maximal intensity is passing through. The same alignment steps are made by opening the vertical gap to a large value and by almost closing the horizontal gap. The next step is so close one gap while the other is at a distance of 10 mm. The closed gap is opened while the detector is scanning the intensity. In general, the intensity is not measured directly when the gaps starts to open due to a tiny misalignment of the offset. Hence, intensity is measured and increasing gradually when the gap is passing a certain gap distance x. From a certain gap distance the intensity starts to saturate. The gap distance x is set to zero position in order to place the zero where no intensity is measured. The other gap distance is aligned in the same way. By repeating the opening process for each gap separately, the distance it set to a position where 80% to 90% of the saturation profile is measured. The distances of the horizontal gap is commonly in the order of 0.5 mm whereby the vertical gap distance is in the order of 1.2 mm It must be noted that the horizontal gap distance is chosen smaller than the vertical one due to the working principle of the Bartels monochromator in the horizontal direction. Therefore, the beam has to be cut by the horizontal gap. The next step is the alignment of the entrance slits (es). Further details of the es alignment will not be included since this alignment is completely analog to the alignment of the monochromator slits.

Thirdly, the sample is moved into the beam path in order to align the sample surface parallel to the beam. This alignment procedure was already explained in section 3.3.2 when the upper crystal surface of each pair I and II (see Fig. 3.3) were aligned parallel to the beam. Therefore, the sample surface can be aligned analog to this method but by moving the om and the say stage instead of the cm1y/cm2y and the cm1th/cm2th stage. However, since the sample surface is parallel to the beam the rotation axis is located along the sample surface.

Finally, the rocking curve of the desired ($h\ k\ l$) plane will recorded in the following way. ω is set to the expected Bragg angle and 2θ is set to twice the Bragg angle. The actual position of the Bragg angle is verified by a rocking scan. If the position of ω and 2θ is set in such a way that the MY_{R1} pixel is located at the maximum of the intensity, the slits are screwed on the tube. The front slit is smaller than the slit right in front of the detector. The reason for this is that the horizontal slits of ms and es affect the beam in such a way that the focus point is located at the sample surface. The vertical slits do not have to be taken into consideration since the Bartels monochromator takes charge of the divergence along the horizontal direction. After the beam is reflected the beam starts to diverge. Therefore, the tube slits function as shields in order to block undesired rays on the detector. Those undesired rays will be discussed in greater detail in section 4. It might be possible that dlin and drot have to be aligned again since the tube slits may cause a complete shading of the beam. After the effort of the alignment it is possible that the rocking curve is recorded.

3.5. Ice Wire Cut

3.5.1. Wire Setup Development

According to [2], the ice surface is disturbed by mechanical treating of the ice crystal. Therefore, in the context of this work a setup was developed to remove the problem of mechanical damage at the surface. The whole setup can be seen in Fig.3.4. In the following the development steps are explained.

Firstly, it must be mentioned that a similar problem has been already treated in doctoral thesis of Schöder (see [3]). Schöder used a current carrying wire in order to thermally cut the ice single crystal. Based on this idea, first tests were carried out to cut frozen tap water with a constantan[3] wire ($\varnothing = 0.3\,\mathrm{mm}$) at room temperature. Two screws were screwed on a metal plate in a distance of roughly 10 cm and were locked with a nut. The screw distance Then the screw threads were isolated with heat-shrink tubing in order to wind both ends of a constantan wire around the screw threads. The wire was winded in such a way that it was under tension. Then a voltage (U) and current (j) were applied between the two ends of the wire. A cylindrical shaped ice piece ($\varnothing = 3.5\,\mathrm{cm}$) was tried to cut along the circle surface with the wire. Although, the ice was cut smoothly at $U = 4.5\,\mathrm{V}$ and $j = 3.2\,\mathrm{A}$ the wire ripped. This can be explained by the heat of fusion L_F of water ($0.33\,\mathrm{MJ\,kg^{-1}}$ [29, p. 660]). At first the ice is heated up to 0 °C by the thermal radiation of the wire. Afterward at the phase transition (solid–liquid) the ice has to absorb the energy ($L_F \cdot \mathrm{mass}$) in order to change the phase to liquid water. During these processes the temperature of the wire is changing. Hence, the wire is expanded and contracted continuously and finally it brake apart. This approach has proved that the electrical and mechanical properties of the constantan wire is not suitable for cutting ice. After comparison of a few wires it turned out that a 80/20 nickel chrome alloy wire is suitable with a diameter of $\varnothing = 0.213\,\mathrm{mm}$ and a resistance of $11.486\,\Omega\,\mathrm{m^{-1}}$ at 20 °C. It turned out that the nickel chrome alloy wire is cutting the ice smoothly at an applied voltage of 8.7 V and a current of 3.3 A.

Besides the selection of the appropriate wire there are two more problems to be solved. The first problem was that the wire has reached a temperature where the heat-shrink tubing melted. The other one was that, the wire was not under tension anymore, when a current was applied due to the thermal expansion of the wire. Both problems were overcome by using springs with two loops. One loop is stuck to the screw thread whereas the other loop is tied to the wire. The other end of the wire is tied to the other spring in such a way that both springs are under tension. Thus, the system is again electrical isolated and the springs avoid that the hot wire melts the isolation. Moreover, the spring compensate the thermal expansion of the wire.

The selection of the springs were made with the constantan wire. The length variation of the wire is roughly $2.9\,\mathrm{cm}$[4] at 6.5 V and 3.4 A. At this voltage and current the wire was glowing red. The spring has to overcome this length variation in such a way that the wire is still under tension. Consequently, the spring constant can be estimated by using Hooke's law. It turned out that a value of roughly $1.5\,\mathrm{N\,m^{-1}}$ would fit. An appropriate spring was found

[3] Constantan is a 40/60 copper nickel alloy [28]
[4] Rough estimation

with 1.601 N m and a length of 18.7 mm. The further development steps are not explained since it would exceed the volume of this work.

The final setup can be seen in Fig. 3.4. The plate (4) where the wire is fixed is moved by the linear step motor (2) along the vertical direction. The function of the height adjuster (1) is to align the X 95 profile (3) along the vertical direction. The plate (5) is located one a slide which in turn is movable along the X 95 profile. A screw on this plate is used to fix the ice on it. The usage of the copper disk The wire (6) is tied up at the springs.

3.5.2. Surface Preparation

In the following the surface preparation of ice will be explained. The ice single crystal bulb is in a freezer at −25 °C. A cylindrical shaped pin with a $\varnothing$= 22 mm and height 36 mm is at room temperature. Then the pin is placed upright in the freezer and after roughly 10 s the ice will be placed on top of the pin in order to melt some of the ice. After roughly 30 s the temperature of the pin is below 0 °C. Hence, the melted ice freezes and the ice stick together with the pin. On the other side of the pin there is a thread It is used to screw on the pin on the plate (5) in Fig. 3.4. The wire setup is placed in the freezer at −25 °C and the sample is screwed on the screw. Then the wire is moved close above the crystal by the motor. Furthermore, the X95 profile is moved to the sample in order to estimate the slice thickness of the ice. The thickness is bounded above since the crystal would touch the plate where the wire is. Afterward, a voltage of 8.7 V and a current of 3.3 A is applied on the wire. With a velocity of roughly 7 mm s^{-1} the wire is moving downwards. After the cutting the slice falls on a foam below. Up to now the surface is not flat enough and can not used in the XRD setup since the alignment would become difficult. Hence, the slice is frozen on a copper disk in the same way as the ice bulb was attached to the pin. Then the copper disk is placed in the wire setup. The wire is aligned to the slice in such a way that the wire would be as close as possible to the surface when moving the wire downwards. The purpose of this alignment is that the radiation of the wire is melting further ice layers when the wire is moved down. If the wire reaches the lower end of the surface it is moved upwards quickly. This procedure was repeated ten times in order to get a flat surface of the sample.

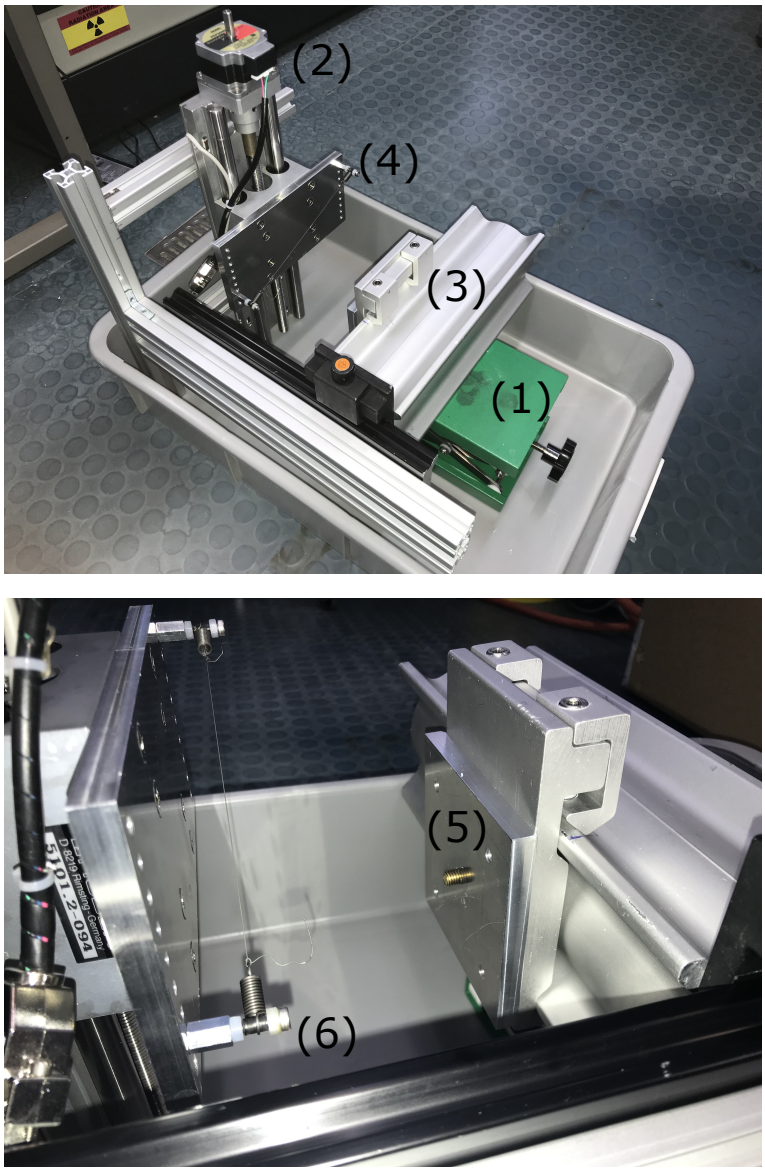

Figure 3.4.: Wire setup for cutting ice with a 80/20 nickel chrome alloy resistance wire.
The upper photo shows an overview of the setup with (1) a height adjuster, (2) the linear motor, (3) X 95 profile system screwed on a slide and (4) the movable plate on the slide of the motor.
The lower photo shows a closer view between the wire and the plate with (5) the movable slide at the X 95 profile, (6) the wire tied up at the springs.

4. Results and Analysis

Einleitung schreiben...

4.1. Results

This section presents the data of the taken measurements of Si and the four ice single crystals in different manners. Furthermore, interpretations of the data are given.

4.1.1. Si (111) Results

In general, a rocking scan is used in order to receive information about the orientations of different domains in a crystal. The result of the taken rocking curve of the Si (1 1 1) plane can be seen in Fig. 4.1. The figure shows the measured intensities of all three pixel intervals in table 3.1. $\Delta\omega := |\omega - 2\theta/2|$ is the so called miscut of the surface. If the (1 1 1) would be perfect parallel to the sample surface the miscut vanishes. An interpolation was done in order to estimate the FWHM. An comparison with Fig. 4.1 shows that the estimated FWHM is roughly 40% larger than the literature value. Moreover, the estimated FWHM of Si is smaller than the intrinsic width of Ge in Fig.A.1a. It might be the reason that the interpolation of the rocking curve in Fig. 4.1 leads to a smaller FWHM. A Gaussian fit might lead to a higher FWHM. Furthermore, all pixel intervals (MY_T, MY_{PB}, MY_{R1}) have approximately the same FWHM. This indicates that the investigated area of Si has no grain boundaries since the lattice spacing is the same. It should be mentioned that the alignment of the sample worked like described in section 3.4. Another method of representing the data can be seen in Fig. 4.2. The two dimensional figure shows on the y-axis the angles ω of the rocking scan. For each ω the intensity of all pixels is plotted along the x-axis. In the following these kind of representation will be called 2D plot. On the x-axis are the pixels or 2θ values. The figure shows only the relevant part of the taken intensity since the rest of the pixels measured low or zero intensity. The streak along the y-axis at roughly $\omega = 14.07°$ shows the divergence of the beam. It is clearly visible that this strike vanishes when ω is not the Bragg regime since most of the intensity is not reflected. Also the diagonal smearing of the intensity is due to the divergence of the beam. Fig. A.9 is the normalized mean value of 100 ω values around the maximal intensity in the 2D plot. ω_{max} is the value where the highest intensity was measured. Then 50 intensity profiles above and below ω_{max} were taken in order to sum all intensities. Afterward, the averaged intensity is normalized by the number of intensity profiles, i.e. 101. The Fig. A.9 shows the already mentioned streak in the 2D plot.

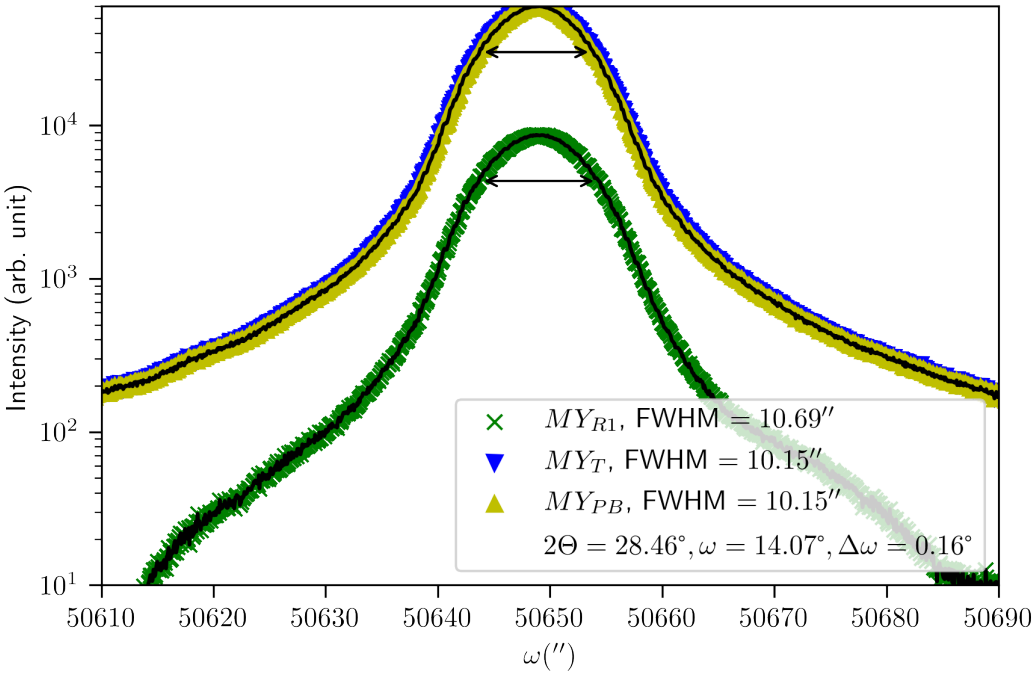

Figure 4.1.: Rocking curve of the Si(1 1 1) plane with 2766 measurement points and a counting time of 10 s in a logarithmic scale. The FWHM is represented by the arrow and the black curve shows the interpolation of the intensity profile.

4.1.2. Basal Face Results

The basal face of four samples were measured. It should be mentioned that the grown ice single crystal have the form of a bulb. The direction of growth is along the c-axis. Hence, a cut perpendicular to the c-axis leads to a surface parallel to the basal face. Moreover, all samples were grown in connection with a collaboration. In addition, the mechanical treated sample surfaces were made by the same collaboration. The surface of sample 0 was prepared with a bandsaw and a microtome. A detailed description of these preparation method is waived since it is explained in detail in [4]. For sample 0 the (0 0 . 2) plane and the (0 0 . 4) were measured at roughly $-17\,°C$. In the contray, only the (0 0 . 2) plane was measured for the remaining samples. Sample 1 was cut with the bandsaw and the rocking curve of the untouched side was measured. It should be mentioned that the alignment of this sample worked had issues since the sample surface was curved. That means that the alignment is not as precise as a flat sample. Hence, the rotation around ω leads to a shift of the illuminated area on the sample. The next sample 2 was prepared like sample 0 but it was never measured since it broke. Another sample 3 was also mechanical treated with the bandsaw and the microtome. Finally, sample 4 was cut with the wire setup and the surface was flatten as described in section 3.5. The measured rocking curves, the 2D plots and the averaged curves can be found in the appendix if they are not explicitly mentioned in this section. A direct comparison of all rocking curves shows

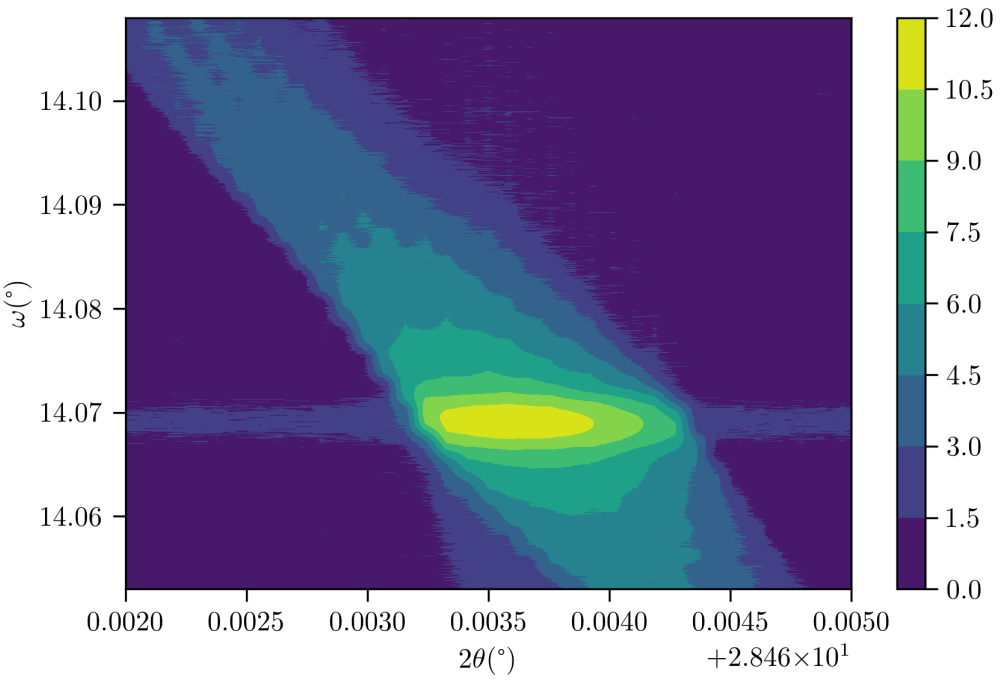

Figure 4.2.: 2D plot of the Si(1 1 1) plane. The intensities are plotted in a logarithmic scale.

that all FWHM are larger than the intrinsic width of the used Bartels monochromator. An interpretation of the 2D map can be explained by Fig. 4.3 since it shows differences compared to Fig. 4.2. The 'V' shaped distributed intensities are due to different lattice spacing values. Furthermore, along the right edge of the 'V' shape small domains are visible. Since the 2θ value is in these domains higher it means that the lattice spacing values are decreased by compression of the ice crystallite within these domains. On the contrary, if a domain is located at smaller 2θ values than the maximum, the domain is expanded. Considering Fig. A.14 it is clear that the domains are the result of the mechanical treatment of sample 1 since the 2D map of sample 4does not show domains and is similar to Fig. 4.2. A direct comparison of Fig. A.14 and Fig. 4.2 shows that the thermal treatment of the ice single crystal is closer to a perfect single crystal than the mechanical treated samples. Also in Fig. 4.5 a shift of the lattice spacing values to higher 2θ values happens since the tail on the right hand side is represent a domain. A streak along the y-axis in Fig. 4.4 is visible but in the mean value in Fig. A.14 it vanishes. The other mean value figures for the other samples do show a streak. This might be another evidence that the thermal treatment leads to less disturbance on the sample surface.

4.1.3. Shift of the melting point

The compressed domains for higher 2θ values leads a shift of the melting point of ice. Therefore, the compressed tension σ is calculated. In general, σ is linear proportional to the relative length change $\Delta d/d$. The so called Young's modulus E is the proportional factor.

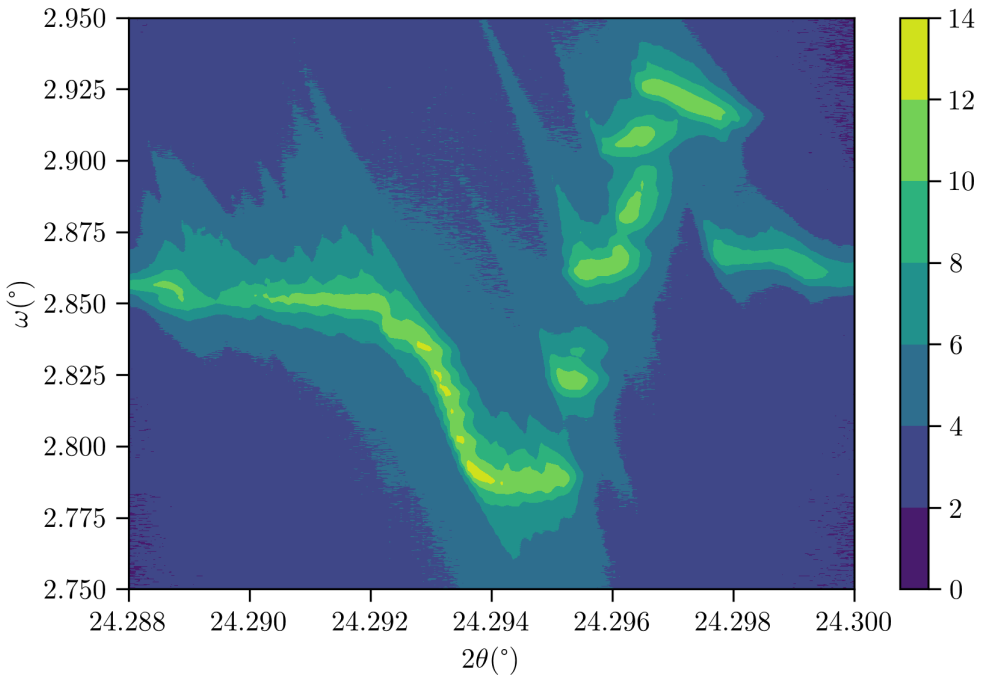

Figure 4.3.: 2D plot of sample 1 ice Ih (0 0 . 2) plane. The intensities are plotted in a logarithmic scale.

Hence, the relation reads as follows

$$\sigma = E \cdot \frac{\Delta d}{d}. \tag{4.1}$$

In order to calculate (4.1) the relative change of q has to be estimated since it is equal to the relative length change. The absolute value of q and Δq can be written as

$$q(2\theta) = \frac{4\pi}{\lambda} \cdot \sin\left(\frac{2\theta}{2}\right)$$
$$\Delta q = \frac{\partial q}{\partial(2\theta)} \cdot \Delta\,(2\theta)\,.$$

Consequently, the relative length change $\Delta d/d$ is connected via (4.2) with the relative change $\Delta q/q$.

$$\frac{\Delta q}{q} = \frac{\cos\,(\theta)}{2\sin\,(\theta)} \cdot \Delta 2\theta = \frac{\Delta d}{d} \tag{4.2}$$

Young's modulus for ice is roughly $E = 9.1$ GPa according to [30]. Hence, the tension can be calculated with (4.1).

The shift of the temperature can be calculated with the so called Clausius–Clapeyron

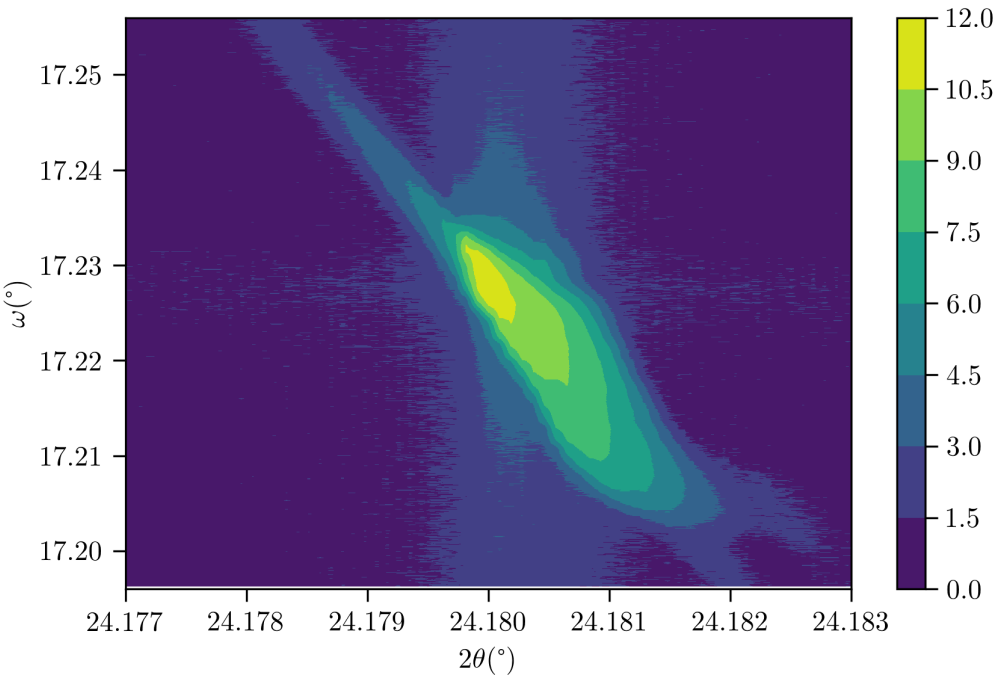

Figure 4.4.: 2D plot of sample 4 ice Ih (0 0 . 2) plane. The surface is prepared with the wire setup at 8.7 V and 3.3 A.2D plot of the Si(1 1 1) plane. The intensities are plotted in a logarithmic scale.

relation in (4.3).

$$\frac{\mathrm{d}T}{\mathrm{d}\sigma} = \frac{\Delta V}{\Delta S} \tag{4.3}$$

Whereby, $\Delta V = 1.634\,\mathrm{cm}^3\,\mathrm{mol}^{-1}$ is volume per mol and the $\Delta S = -22\,\mathrm{J\,mol}^{-1}\,\mathrm{K}^{-1}$ is the enthalpy according to [**?**]. The ice can be treated with (4.3) since the temperature is close below 0 °C and therefore near the coexistence curve of liquid water. Furthermore, the lefthand side of (4.3) changes to $\Delta T/\Delta\sigma$.

Considering again the 2D map in Fig. 4.3. The very right green spot at 24.3° and the maximum intensity 24.294° have an angular distance $2\theta = 0°$. The tension can be calculated by using (4.1) and (4.2). The shift of the melting point can be calculated by (4.3). The result can be read in table 4.1 where also other examples are given in order to compare the results.

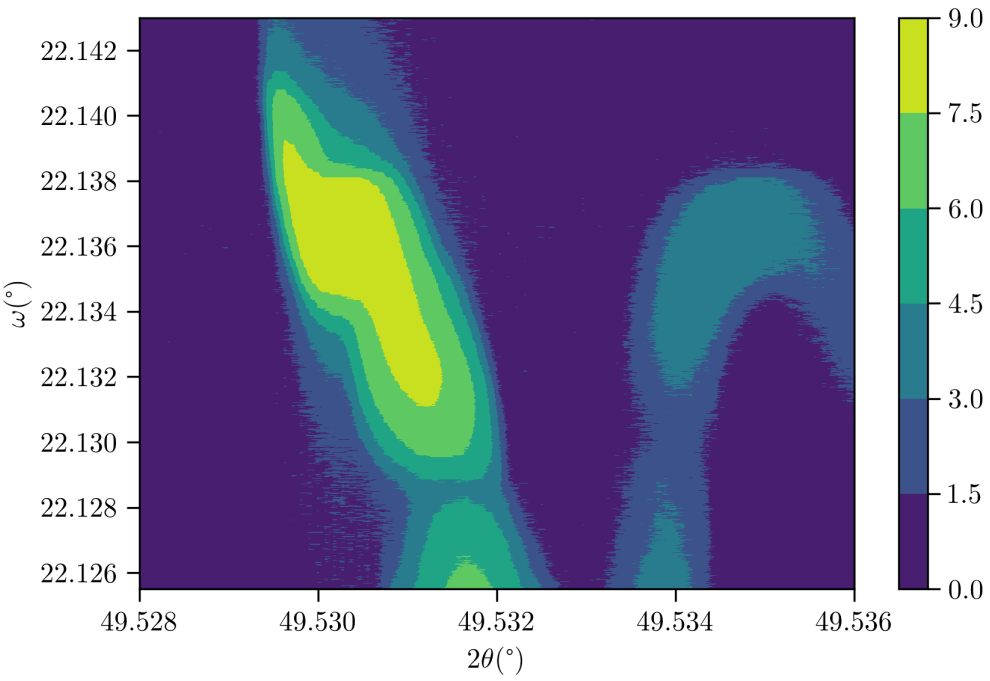

Figure 4.5.: 2D plot of sample 0 ice Ih (0 0 . 4) plane.

Table 4.1.: Estimated tensions and shifts of the melting point for selected samples.

Sample	$(h\,k\,.\,l)$	σ(N mm^{-2})	ΔT(°C)
0	(0 0 . 2)	-27	2
0	(0 0 . 4)	-71	5.26
1	(0 0 . 2)	-61	4.55
4	(0 0 . 2)	-17	1.3

It can not be said if the values are close to the reality since no comparative data are available. Only a trend is recognizable that the shift of the melting point for sample 4 is the lowest.

5. Discussion and Outlook

The first task of this work was the alignment of the Bartels monochromator and the slit system in order to reduce the divergence of the produced beam. Furthermore, the realization of the wire setup was accomplished, since in the paper of Bilgram [2] mechanical treatment disturbs the ice single crystal up to 1 cm below the surface. The development of the wire setup was done by me with the support of my supervisor Markus Mezger and my work colleagues. A further task was the surface preparation of the ice single crystal with the wire setup. I received the grown crystal with a collaboration of *The Water at Interfaces* group in the MPIP. Afterward, I performed the surface preparation. Additionally, the alignment of the XRD setup in order to obtain the rocking curves. Also this time, I received assistance from Markus Mezger since the XRD setup requires technical understanding.

It has not been necessary to know the exact temperature of the ice sample. Nevertheless, it might be necessary in the future if further knowledge is gained.

The development of the wire setup has still problems which we are facing. Firstly, the cables for the power supply starts to shake during a cutting procedure. This may cause a ripple pattern on the ice surface since the cables forward their movement to the wire. Therefore, it can not guaranteed that the ice is not treated mechanically. Secondly, the liquid water runs downwards and freezes again at the bottom of the surface. This leads to stalactite shaped ice pin. This pin can grow to the bottom of the freezer and then the pin has to break apart. Thirdly, the number of springs can be increased. Then the wire is threaded through the loops in a zigzag pattern. The result is that effective heating area causes less refreezing of liquid water on the surface. The requirement for several springs is that the loops of each spring has to be orientated by 90° to each other. Hence, all wire strings lay on a plane. Thus, the thermal radiation causes a flat surface. As it can be seen in Fig.3.4 the loops are parallel. Although the problem of the loop orientation was known but because of delivery problems no new loops could be ordered in time.

The result of the thermally treated ice single crystals confirmed the expectation that the grain boundaries are not as distinct as the mechanical treated ones. This shows the direct comparison between the data of the two different prepared ice crystals and the Si (1 1 1) plane. Further calculations shows that the tension and the shift of the melting point within a ice crystallite depends strongly on the surface preparation. These calculation were based on the assumption that the Clausius–Clapeyron relation can be used since the temperature is slightly below 0 °C.
For the lack of time only one thermally treated sample was prepared. Consequently, the results are based on one data set. It would be interesting to know, if the data of more thermally

prepared samples would lead to the same result.

A. Appendix

A.1. Tables

Table A.1.: Characteristics of Ge crystals for a twofold and fourfold monochromator from [26, p. 113]

Method of operating	$(h\,k\,l)$	FWHM	Relative Intensity based on 100
Fourfold	(2 2 0)	12″	1
Fourfold	(4 4 0)	5″	0.08
Twofold	(2 2 0)	600″	3
Twofold	(4 4 0)	250″	.03

Table A.2.: Characteristics of typical monochromator crystals from [26, p. 111]

Crystal	(hkl)	d_{hkl}[nm]	2θ[°]	$\lvert F^2\rvert$	D_x[gcm^{-}3]	d(95%)[µm]
Graphite	(0 0 0 2)	0.33756	26.382	299.5	2.281	363.30
Quartz	(1 0 $\bar{1}$ 1)	0.33435	26.640	874.8	2.649	38.80
LiF	(2 0 0)	0.20130	44.997	927.1	2.638	190.70
$CaCO_3$	(1 1 0)	0.24940	35.966	4854	2.711	24.45
NaCl	(2 0 0)	0.28210	31.613	7197	2.163	25.04
Si	(1 1 1)	0.31355	28.443	3551	2.329	26.41
Si	(4 0 0)	0.13577	69.132	3611	2.329	61.00
Ge	(1 1 1)	0.32660	27.284	23966	5.325	9.47
Ge	(2 2 0)	0.20000	45.306	36246	5.325	15.86
Ge	(4 4 0)	0.10000	100.761	16831	5.325	31.72

Table A.3.: Characterization of electron, neutron and X-radiations from [17, p. 7]

Characteristic	Electrons	Neutrons	X-rays
Absorption	high	very low	low
Penetration	< 1 µm	cm	mm
Rocking curve width	degree	<arc second	<arc second
Strain sensitivity	10^{-3}	10^{-7}	10^{-7}
Spatial resolution	1 nm	30 µm	1 µm
Destructive?	yes	mo	no
Cost	high	very high	medium
Convenience	good	poor	good

Table A.4.: Calculated angles and **q** components for selected (hk.l) planes from [4]. The d-spacing values are taken from [21].

Reflection plane	$2\theta(^\circ)$	d_{hkl}(Å)	q(Å^{-1})	$q_\parallel$(Å^{-1})	$q_\perp$(Å^{-1})	$\delta(^\circ)$	$\omega(^\circ)$	$\chi(^\circ)$	$\phi(^\circ)$
(0 0 . 2)	24.29	3.66	1.716	0	1.716	12.15	12.15	0	–
(1 0 . 5)	68.38	1.37	4.584	1.613	4.290	54.80	0	0	0
(1 0 . 5)	68.38	1.37	4.584	1.613	4.290	54.80	0	0	60
(1 0 . 0)	22.81	3.89	1.613	0	1.613	11.41	11.41	0	–
(2 0 . 0)	46.60	1.95	3.226	0	3.226	23.30	23.30	0	–
(2 0 . 1)	48.32	1.88	3.338	0.858	3.226	39.05	9.27	0	180
(1 1 . 0)	40.06	2.25	3.338	0.858	3.226	39.05	9.27	0	180

A.2. Figures

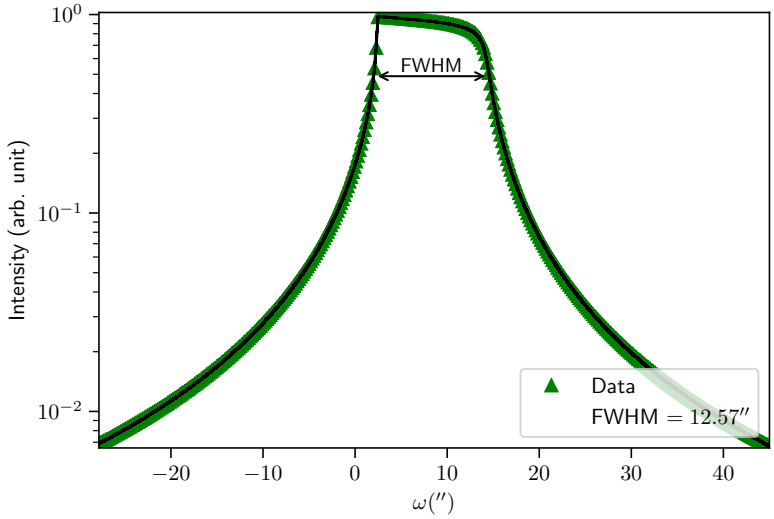

(a) Rocking curve of Ge(2 2 0) plane. The interpolation is drawn in black and the arrows marking the FWHM.

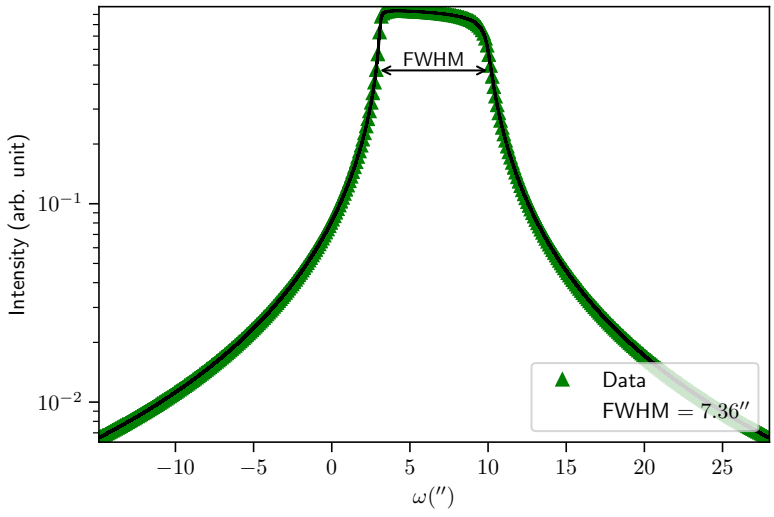

(b) Rocking curve of Si(1 1 1) plane. The interpolation is drawn in black and the arrows marking the FWHM.

Figure A.1.: Measured rocking curve of Ge(2 2 0) (a) and Si(1 1 1) (b) in log scale. The beam is σ polarized Cu-K_α radiation, $\lambda = 1.54$ Å, $E = 1.54$ keV. Data from [27].

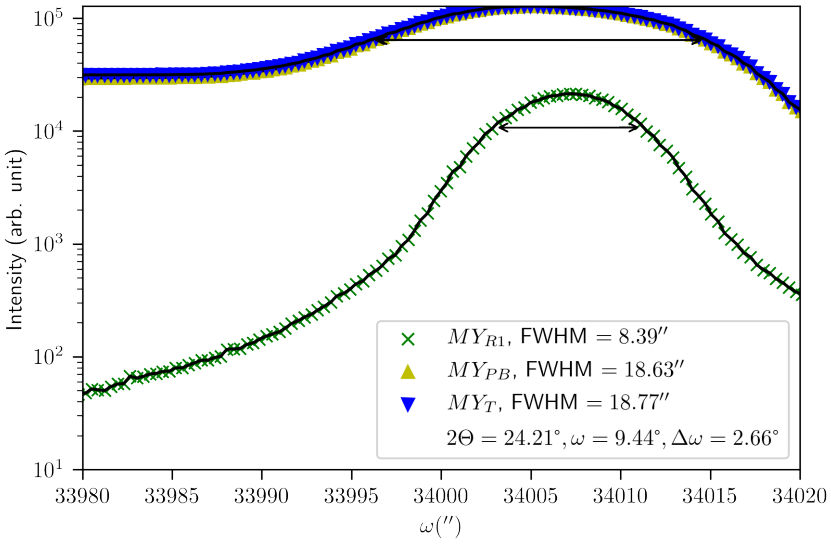

Figure A.2.: Rocking curve of sample 0 ice Ih basal face (0 0 . 2) plane with 1600 measurement points and a counting time of 20 s in a logarithmic scale with a 6 mm slit in front of the tube. The FWHM is represented by the arrow and the black curve shows the interpolation of the intensity profile.

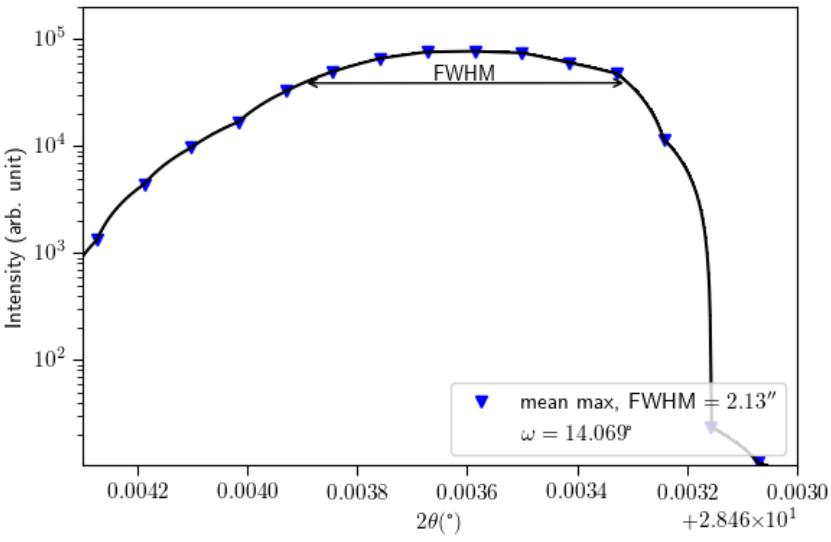

Figure A.9.: Calculated mean value of the Si (1 1 1) plane. The interpolation is drawn in black and the arrows marking the FWHM.

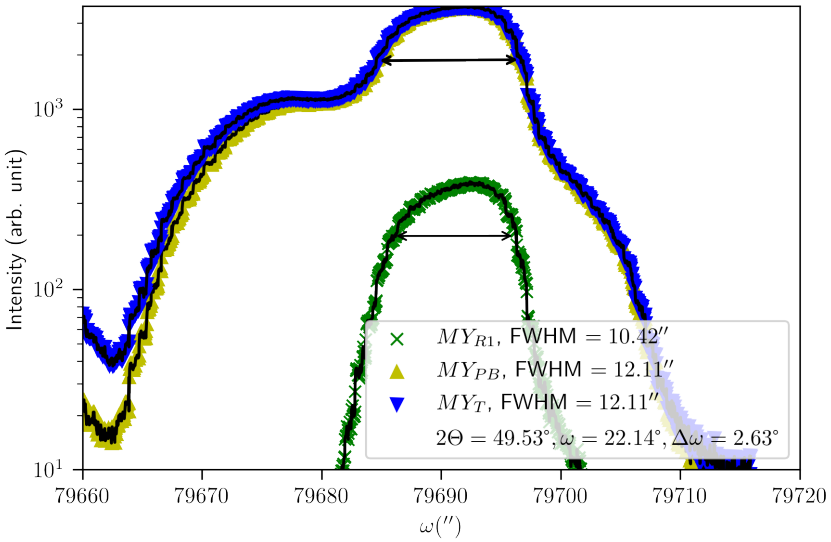

Figure A.3.: Rocking curve of sample 0 ice Ih basal face (0 0 . 4) plane with 1600 measurement points and a counting time of 20 s in a logarithmic scale with a 6 mm slit in front of the tube. The FWHM is represented by the arrow and the black curve shows the interpolation of the intensity profile.

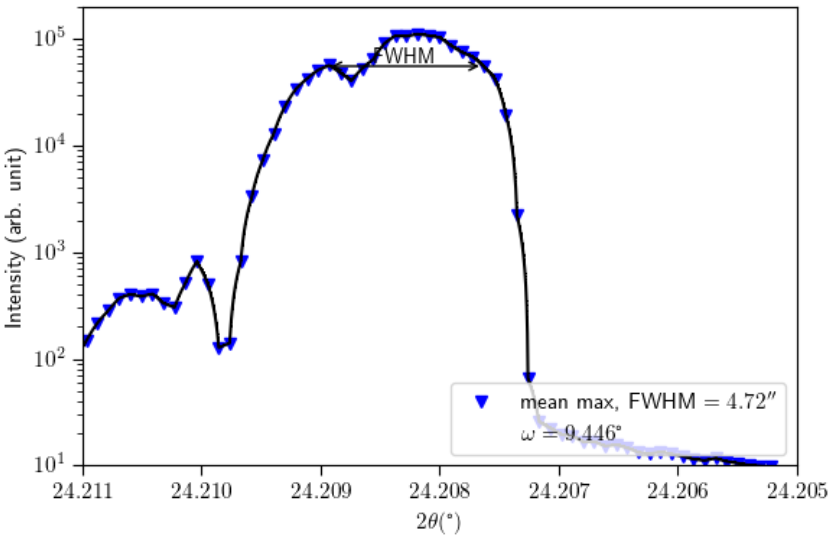

Figure A.10.: Calculated mean value of sample 0 ice Ih (0 0 . 2) plane. The interpolation is drawn in black and the arrows marking the FWHM.

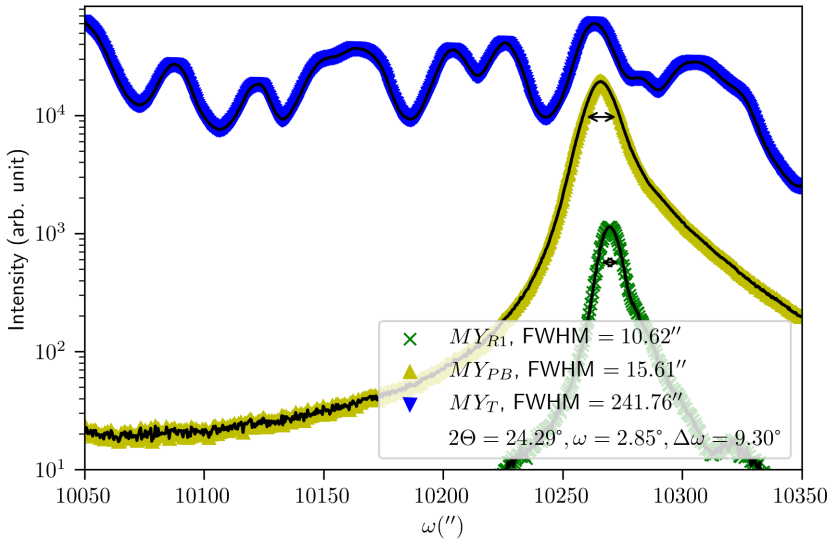

Figure A.4.: Rocking curve of sample 1 ice Ih basal face (0 0 . 2) plane with 2800 measurement points and a counting time of 20 s in a logarithmic scale. The FWHM is represented by the arrow and the black curve shows the interpolation of the intensity profile.

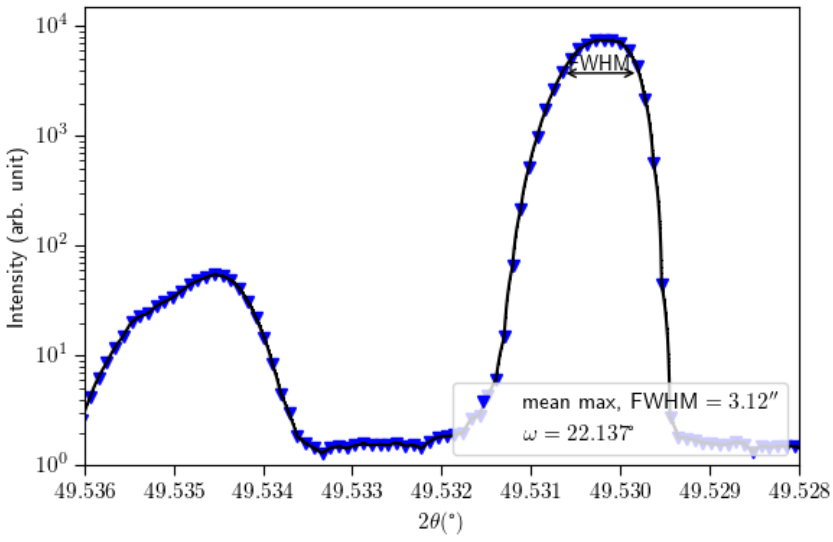

Figure A.11.: Calculated mean value of sample 0 ice Ih (0 0 . 4) plane. The interpolation is drawn in black and the arrows marking the FWHM.

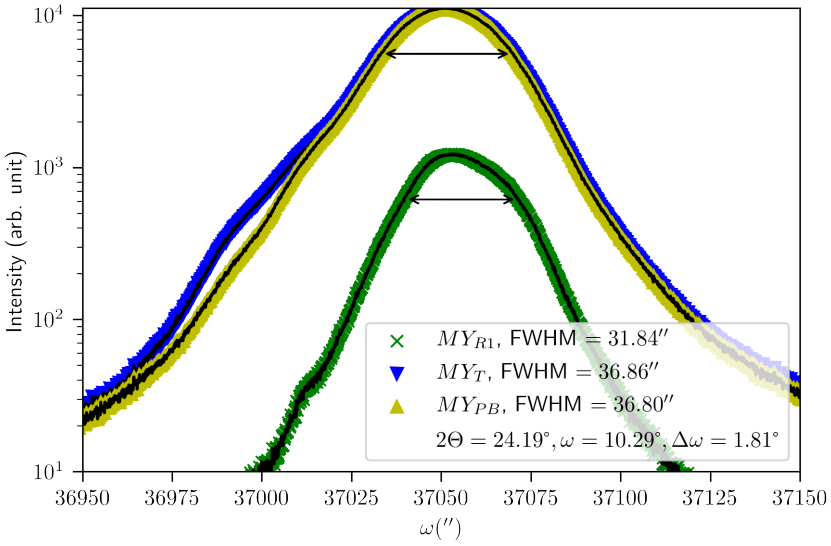

Figure A.5.: Rocking curve of sample 3 ice Ih basal face (0 0 . 2) plane with 2100 measurement points and a counting time of 20 s in a logarithmic scale. The FWHM is represented by the arrow and the black curve shows the interpolation of the intensity profile.

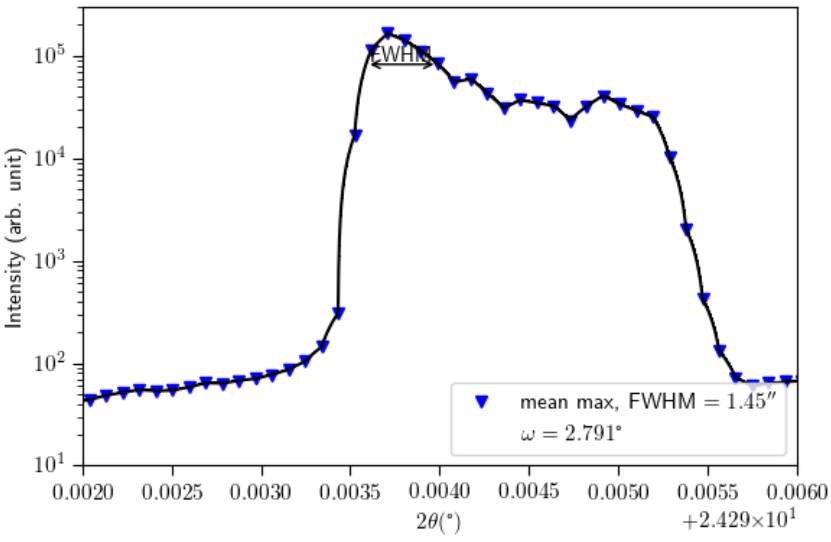

Figure A.12.: Calculated mean value of sample 1 ice Ih (0 0 . 2) plane. The interpolation is drawn in black and the arrows marking the FWHM.

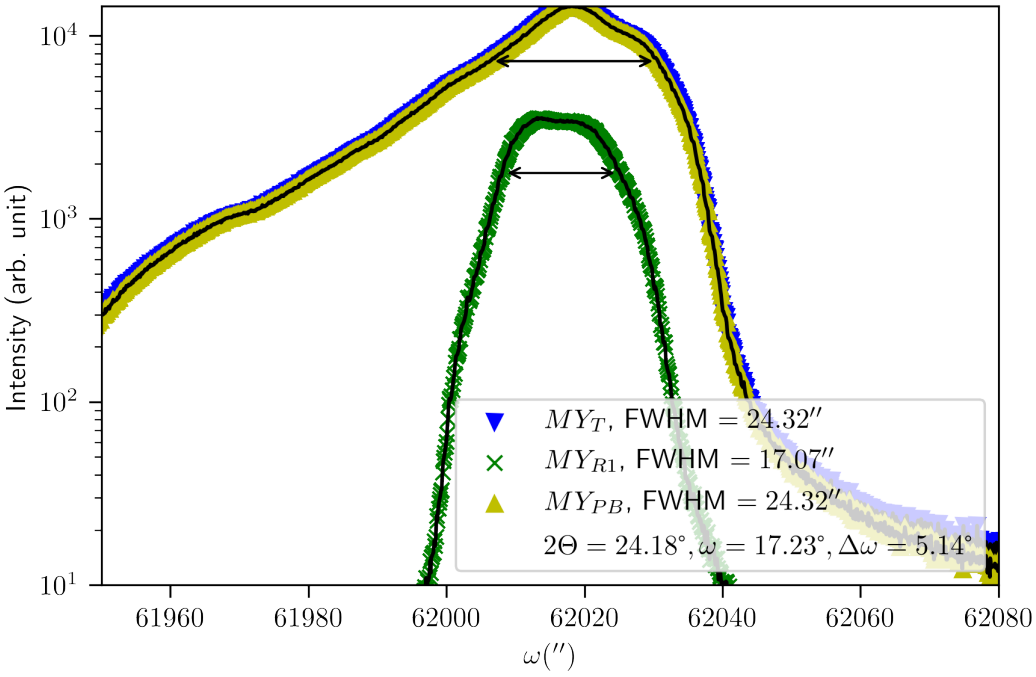

Figure A.6.: Rocking curve of sample 4 ice Ih (0 0 . 2) plane with 2000 measurement points and a counting time of 20 s in a logarithmic scale with a 2 mm slit and a 4 mm slit at front and the end of the tube, respectively. The FWHM is represented by the arrow and the black curve shows the interpolation of the intensity profile.

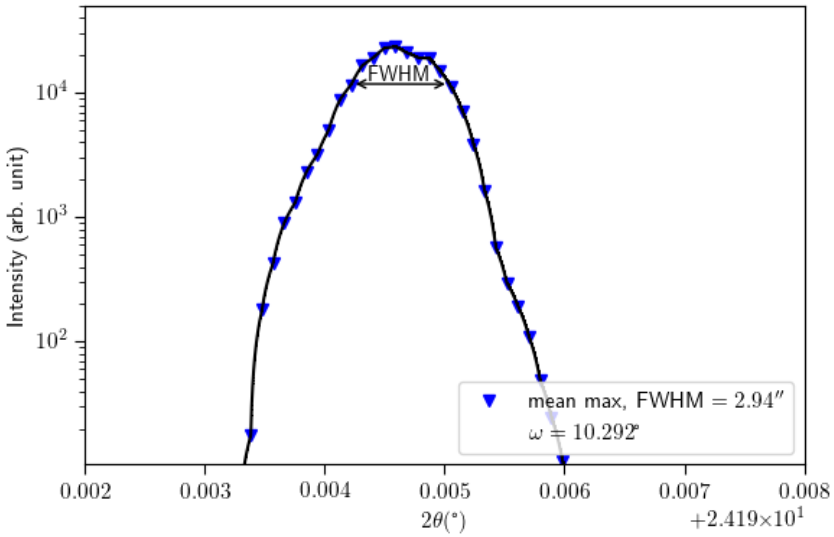

Figure A.13.: Calculated mean value of sample 3 ice Ih (0 0 . 2) plane. The interpolation is drawn in black and the arrows marking the FWHM.

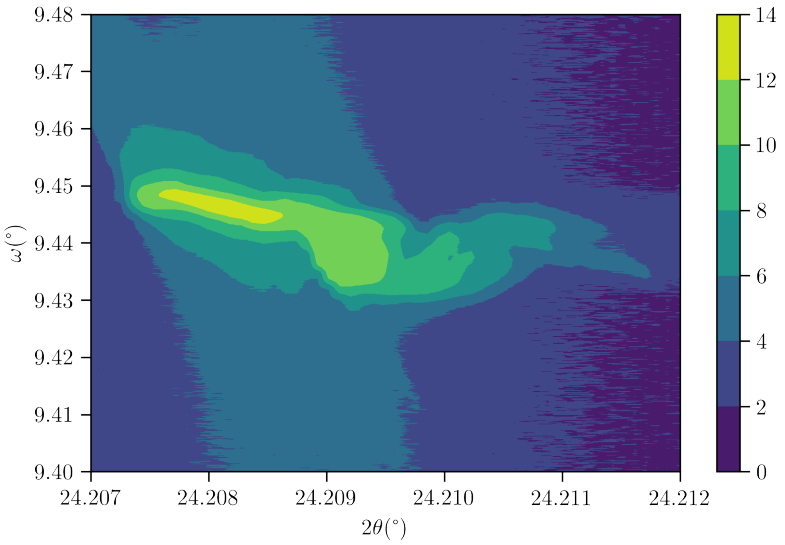

Figure A.7.: 2D plot of sample 0 ice Ih (0 0 . 2) plane. The intensities are plotted in a logarithmic scale.

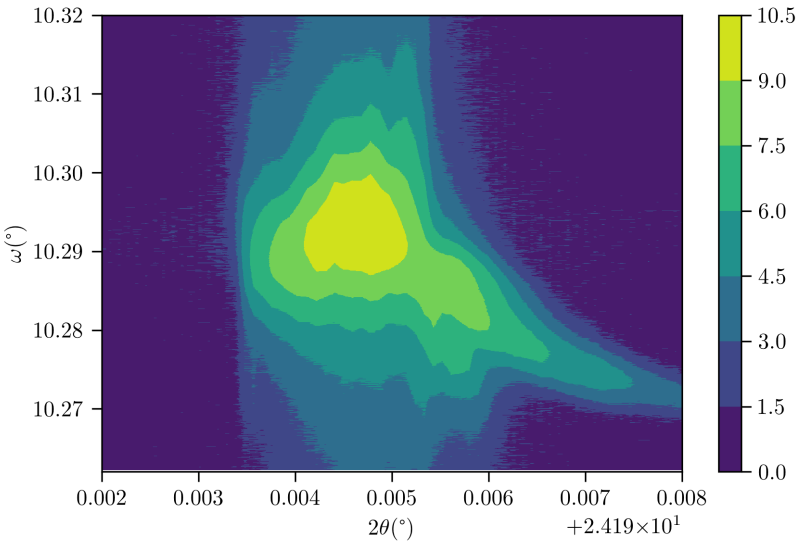

Figure A.8.: 2D plot of sample 3 ice Ih (0 0 . 2) plane. The intensities are plotted in a logarithmic scale.

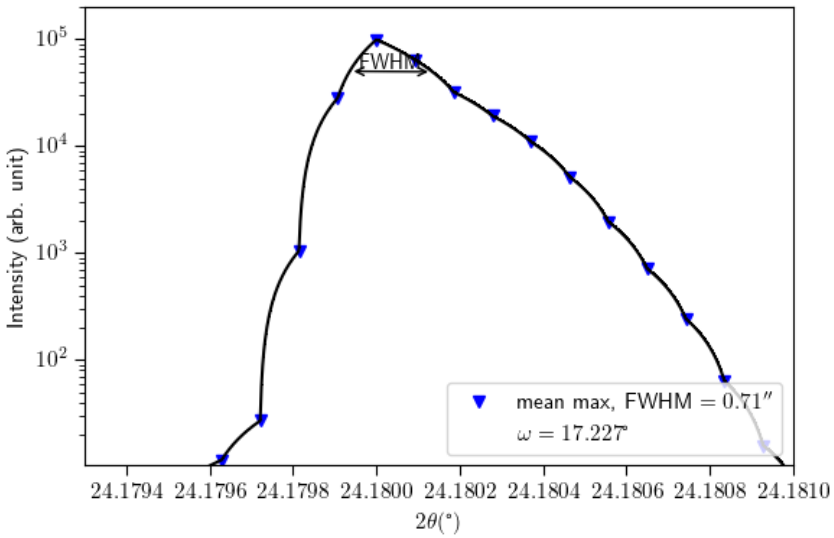

Figure A.14.: Calculated mean value of sample 4 ice Ih (0 0 . 2) plane. The interpolation is drawn in black and the arrows marking the FWHM.

List of Figures

List of Tables

Bibliography

[1] M. Peplow, "Graphene sandwich makes new form of ice," 2015, visited on 16.11.2018. [Online]. Available: https://www.nature.com/news/graphene-sandwich-makes-new-form-of-ice-1.17175

[2] J. Bilgram, H. Wenzl, and G. Mair, "Perfection of zone refined ice single crystals," *Journal of Crystal Growth*, vol. 20, no. 4, pp. 319–321, 1973. [Online]. Available: https://doi.org/10.1016/0022-0248(73)90100-0

[3] S. Schöder, "Substrate-dependence of the ice premelting at heterogeneous interfaces: an x-ray scattering study," 2008. [Online]. Available: http://dx.doi.org/10.18419/opus-6669

[4] M. A. Sánchez, T. Kling, T. Ishiyama, M.-J. van Zadel, P. J. Bisson, M. Mezger, M. N. Jochum, J. D. Cyran, W. J. Smit, H. J. Bakker *et al.*, "Experimental and theoretical evidence for bilayer-by-bilayer surface melting of crystalline ice," *Proceedings of the National Academy of Sciences*, vol. 114, no. 2, pp. 227–232, 2017.

[5] M. Born, "Quantenmechanik der Stoßvorgänge," *Zeitschrift fur Physik*, vol. 38, pp. 803–827, Nov. 1926.

[6] J. Als-Nielsen and D. McMorrow, *Elements of modern X-ray physics*. John Wiley & Sons, 2011.

[7] H. Ibach and H. Lüth, *Festkörperphysik: Einführung in die Grundlagen*. Springer-Verlag, 2009. [Online]. Available: http://dx.doi.org/10.1007/978-3-540-85795-2

[8] T. Butz, *Fouriertransformation für Fußgänger*. Springer, 2012. [Online]. Available: http://dx.doi.org/10.1007/978-3-8348-8295-0

[9] D. Meschede, *Gerthsen physik*. Springer-Verlag, 2015. [Online]. Available: http://dx.doi.org/10.1007/978-3-662-45977-5

[10] W. Massa, "Kristallstrukturbestimmung," Wiesbaden, pp. XII, 243 S., 2015. [Online]. Available: http://dx.doi.org/10.1007/978-3-658-09412-6

[11] W. Borchardt-Ott, "Die 7 Kristallsysteme," *Kristallographie: Eine Einführung für Naturwissenschaftler*, 2009.

[12] P. Ewald, "Introduction to the dynamical theory of x-ray diffraction," *Acta Crystallographica Section A: Crystal Physics, Diffraction, Theoretical and General Crystallography*, vol. 25, no. 1, pp. 103–108, 1969.

[13] P. Dobrinski, G. Krakau, and A. Vogel, *Physik für Ingenieure*. Springer, 2010. [Online]. Available: http://dx.doi.org/10.1007/978-3-8351-9076-4

[14] A. Authier, *Dynamical theory of X-ray diffraction*. Oxford University Press on Demand, 2004, vol. 11. [Online]. Available: http://dx.doi.org/10.1093/acprof:oso/9780198528920.001.0001

[15] A. Guinier, *X-ray diffraction: In Crystals, Imperfect Crystals, and Amorphous Bodies*. Dover Publications, Inc. New York, 1964.

[16] A. M. Afanas'ev and I. P. Perstnev, "On the bragg reflexion from ideal absorbing crystals," *Acta Crystallographica Section A*, vol. 25, no. 4, pp. 520–523, 1969. [Online]. Available: https://onlinelibrary.wiley.com/doi/abs/10.1107/S0567739469001100

[17] D. K. Bowen and B. K. Tanner, *High resolution X-ray diffractometry and topography*. CRC press, 2005.

[18] J. D. Bernal and R. H. Fowler, "A theory of water and ionic solution, with particular reference to hydrogen and hydroxyl ions," *The Journal of Chemical Physics*, vol. 1, no. 8, 1933.

[19] V. F. Petrenko and R. W. Whitworth, *Physics of ice*. OUP Oxford, 1999.

[20] W. Kuhs and M. Lehmann, "The structure of ice-ih," *Water science reviews*, vol. 2, pp. 1–65, 1986.

[21] R. Downs, K. Bartelmehs, G. Gibbs, and M. Boisen, "Interactive software for calculating and displaying x-ray or neutron powder diffractometer patterns of crystalline materials," pp. 1104–1107, 1993, visited on 24.10.2018. [Online]. Available: http://rruff.geo.arizona.edu/AMS/xtal_data/DIFfiles/15878.txt

[22] K. Kopitzki, P. Herzog, and P. Herzog, *Einführung in die Festkörperphysik*. Springer, 2017. [Online]. Available: http://dx.doi.org/10.1007/978-3-662-53578-3

[23] R. Unkelbach, "Röntgenuntersuchungen zur Textur von Eis-Komposit Materialien," 2018.

[24] J. Sólyom, *Fundamentals of the Physics of Solids: Volume 1: Structure and Dynamics*. Springer Science & Business Media, 2007, vol. 1.

[25] M. Mezger.

[26] L. Spieß, G. Teichert, R. Schwarzer, H. Behnken, and C. Genzel, *Moderne röntgenbeugung: röntgendiffraktometrie für Materialwissenschaftler, Physiker und Chemiker*. Springer-Verlag, 2009.

[27] S. Stepanov, accessed: 09.11.2018. [Online]. Available: http://x-server.gmca.aps.anl.gov/cgi/www_form.exe?template=x0h_form.htm

[28] D. R. Askeland, P. P. Fulay, and W. J. Wright, *The science and engineering of materials*. Christopher M. Shortt, 2010.

[29] D. C. Giancoli, *Physik: Lehr-und Übungsbuch*. Pearson Deutschland GmbH, 2010, vol. 4023.

[30] D. R. H. Jones and M. F. Ashby, *Engineering materials 2: an introduction to microstructures and processing*. Butterworth-Heinemann, 2012.